Global and Planetary Change 184 (2020) 103045

Contents lists available at ScienceDirect

Global and Planetary Change

journal homepage: www.elsevier.com/locate/gloplacha

Research article

Late Pleistocene oceanographic and depositional variations along the Wilkes Land margin (East Antarctica) reconstructed with geochemical proxies in deep-sea sediments

Francisco J. Jimenez-Espejo[a,b,*], Massimo Presti[c], Gerhard Kuhn[d], Robert Mckay[e], Xavier Crosta[f], Carlota Escutia[a], Renata G. Lucchi[c], Raffaella Tolotti[g], Toshihiro Yoshimura[b], Miguel Ortega Huertas[h], Patrizia Macrì[i], Andrea Caburlotto[c], Laura De Santis[c]

[a] Instituto Andaluz de Ciencias de la Tierra (CSIC-UGR), Armilla, Spain
[b] Department of Biogeochemistry, Japan Agency for Marine-Earth Science and Technology (JAMSTEC), Yokosuka, Japan
[c] Istituto Nazionale di Oceanografia e Geofisica Sperimentale (OGS), Trieste, Italy
[d] Alfred-Wegener-Institut Helmholtz-Zentrum für Polar- und Meeresforschung (AWI), Bremerhaven, Germany
[e] Antarctic Research Centre, Victoria University of Wellington, Wellington, New Zealand
[f] UMR-CNRS 5805 EPOC, Université de Bordeaux, France
[g] DISTAV, Università degli Studi di Genova, Italy
[h] Departamento de Mineralogía y Petrología, Universidad de Granada, Spain
[i] Istituto Nazionale di Geofisica e Vulcanologia (INGV), Rome, Italy

ARTICLE INFO

Keywords:
Wilkes Land
Glaciation
Antarctic Bottom Water
Redox
Manganese

ABSTRACT

Water masses and depositional environments over the last 500 ka were reconstructed using absolute and relative abundances of lithogenous, biogenous and redox-sensitive elements in four sediment cores from two channel-levee systems of the Wilkes Land continental slope (East Antarctica). Sediments older than the Mid-Bruhnes event (MBE, 430 ka BP) show reduced glacial/interglacial variability in the abundance of elements associated to the terrigenous mineral phases (i.e. Al, Ti, Fe and partly Si). This suggests minor ice-sheet size changes occurred in the Antarctic margin during the pre-MBE "lukewarm" interval. Post-MBE sediments record instead a high variability between glacial and interglacial periods in the concentration of terrigenous and biogenous (i.e. Ca, Ba) elements suggesting larger amplitude changes in both ice-sheet size and ocean conditions toward the gradual establishment of last glacial cycle conditions. Moreover, a marked increase of Mn during the glacial to interglacial transitions, indicates a post-depositional migration of the redox front and re-oxidation of the surface sediment layers linked to major changes in bottom water oxygen conditions associated to Antarctic Bottom Water formation along the margin at the onset of deglaciations.

1. Introduction

Deep Southern Ocean water conditions played a major role on the planetary atmospheric CO_2 levels over the glacial-interglacial cycle whereby the colder, saltier and less ventilated abyssal Southern Ocean stored higher quantities of CO_2 during glacial periods (e.g., Adkins, 2013; Ferrari et al., 2014; Ronge et al., 2015; Pedro et al., 2016; Kohfeld and Chase, 2017; Wagner and Henry, 2017). However, little is known about the evolution of deep Southern Ocean water masses, which until now has been mainly reconstructed from mid-low latitudes because of the scarcity of records in the Antarctic margins source regions.

The Adélie Land and George V Land (AL-GVL) sectors of the East Antarctic Ice Sheet (EAIS) are the third major source region of Antartic Bottom Waters (AABW) formation after the Weddell and Ross seas (Rintoul, 1998, 2007). Modern observations indicate reduced formation and freshening of regional High-Salinity Shelf Water (HSSW) (Lacarra et al., 2014; Campagne, 2015; Fogwill et al., 2017) and AABW (Rintoul, 2007; Purkey and Johnson, 2012), partly due to the melting of circum-Antarctic ice shelves and glaciers (Miles et al., 2013). Of particular importance, both ice mass loss (e.g, Shen et al., 2018; Rignot et al., 2019) and melting of the Antarctic ice sheet are predicted to increase over the next century with further implications for sea-level rise (Golledge et al., 2015; Ritz et al., 2015) and AABW dampening

* Corresponding author at: Instituto Andaluz de Ciencias de la Tierra (CSIC-UGR), Armilla, Spain.
E-mail address: fjjspejo@ugr.es (F.J. Jimenez-Espejo).

https://doi.org/10.1016/j.gloplacha.2019.103045
Received 20 May 2019; Received in revised form 18 September 2019; Accepted 24 September 2019
Available online 18 October 2019
0921-8181/

(Williams et al., 2016). Giving its relevance, it appears essential to document past changes in AABW in AL-GVL region. Although some information exists about the Holocene evolution of bottom water circulation regime in AL-GVL (Harris and Beaman, 2003; Presti et al., 2003, 2005; Bostock et al., 2013), the dynamic of coastal glaciers (Crespin et al., 2014; Crosta et al., 2018) and the seasonal sea-ice cycle (Denis et al., 2010), the complex interactions between these climatic components is poorly constrained, especially on longer timescales (Sen Gupta et al., 2009).

Sedimentation on the continental rise of the AL-GVL area is very much linked to the evolution of such water masses through time. Turbidity currents, triggered by sediment failure at the continental shelf edge, can be affected by subsequent reworking by downslope cascading of density currents and/or along-slope contour currents, as well as rainout of pelagic biogenic oozes and ice rafted debris (IRD). All these processes varied significantly through glacial/interglacial cycles of the Plio-Pleistocene, as the ice sheet expanded to the continental shelf edge during glacials and subsequently retreated during interglacials (Escutia et al., 2011; Cook et al., 2013; Reinardy et al., 2015; Patterson et al., 2014). However, a detailed understanding of how water mass formation along the Wilkes Land varied through Late Pleistocene climate changes and how it is manifested in the sedimentary record, is still missing and will be the focus of this work.

The abundances of specific major and trace elements of marine sediments, together with sedimentary and biostratigraphic proxies, provide for reconstructions of past oceanographic and depositional conditions (e.g. Lyons et al., 2003; Sageman et al., 2003; Algeo and Maynard, 2004; Nameroff et al., 2004; Tribovillard et al., 2006; Calvert and Pedersen, 2007; Crosta and Koç, 2007; Tolotti et al., 2017). In this paper, we compare the patterns of sediment chemical elements (Al, Ti, Fe, Ba, Ca, Mn and Mo) from a suite of sediment cores collected on the continental rise offshore the Adélie and George V Land sectors, to reconstruct the evolution of water masses in the Antarctic margin relating to late Pleistocene changes of the regional ice sheet size on the continental shelf.

2. Oceanography and bathymetry of the study area

The Adélie Land Bottom Water (ALBW) represents the Wilkes Land contribution to AABW (Foster and Carmack, 1976) and can be traced from its source region on the continental shelf between 142.5 °E and 145.5 °E (Rintoul, 1998) throughout a large area of the abyssal ocean (Mantyla and Reid, 1983). The ALBW forms in particular conditions, when cold and dense shelf water is produced by brine rejection in polynyas under enhanced sea ice production. Dense waters, having negative buoyancy with respect to the ambient water masses, spreads across shelf sills, and flows down the continental slope, funnelled into slope canyons, to produce the AABW (Baines and Condie, 1998; Bindoff et al., 2001; Williams and Bindoff, 2003). Sediments transferred from the shelf to the slope area, are then affected by the westerly flowing Antarctic Slope Current (ASC) , this process promotes fine particle winnowing and characteristic mixed turbidite and contourite deposits, already described in different location of the Antarctic margin (e.g., Escutia et al., 2002; Lucchi et al., 2002; Escutia et al., 2005; Lucchi and Rebesco, 2007; Hillenbrand et al., 2008).

Significant changes in bottom water properties can occur in the presence of complex bathymetry over the continental slope and rise in addition to strong seasonal variations (Aoki et al., 2005). Mooring observations on the continental rise near 140°E between 1995 and 1996 (Fukamachi et al., 2000) detected cold, bottom currents with intensified activity during winter and spring, penetrating the deep ocean area as cascading dense plumes (Baines, 2008; Williams et al., 2010) and steered by topographic features such as channels and levees (Fig. 1) (Fukamachi et al., 2000; Caburlotto et al., 2006; De Santis et al., 2007; Baines, 2008; Williams et al., 2010).

The upper slope of the Wilkes Land continental margin is incised by numerous gullies (Fig. 1) that converge into deeply incised submarine canyons at about 1000 m water depth (Beaman et al., 2011). At a water depths of 2500 and 3600 m, distinct asymmetrical mounds are present between canyons. Such mounds are characterized by a gentle eastern side and a steeper western side forming a well-defined channel-levee system (Escutia et al., 2000; Caburlotto et al., 2006). Seismic investigations of the area, indicate that the deep-sea channels are the product of erosion by down-slope gravity flows, that move preferentially along the channels connected to the upper slope, representing also the preferential ways trough which dense deep-water flows (Escutia et al., 2000; Donda et al., 2003; Caburlotto et al., 2006). The channel-levee systems originated during the Cenozoic from an interplay of fine-grained turbidity flows travelling though the channels, material transported down-slope in benthic nepheloid layers and off-slope in intermediate nepheloid layers, plus hemipelagic deposition (Escutia et al., 2000, 2005; De Santis et al., 2003; Donda et al., 2003). A component of the finer-grained material may eventually become entrained and reworked by westward, along-slope (contour) bottom currents and deposited mainly on the gentler slope of the levees distal to the channel axis, and in the lower relief levee systems in water depths below 3500 m. This interaction of sedimentary processes explains the asymmetry of the ridges and their internal depositional structure (Escutia et al., 2000, 2005; De Santis et al., 2003; Donda et al., 2003, 2007).

3. Materials and methods

3.1. Core location and description

The four piston cores examined for this study were (Table 1):

Core MOGAM06-01 (length 4 m) was recovered from 2600 m water depth, on the western side of the WEGA channel during PNRA MOGAM expedition, in 2006 (De Santis and Expedition Scientists, XXI PNRA expedition, 2006).

Core WEGA PC20 (length 4.63 m) was recovered from a depth of 3014 m, about 80 km downslope from the MOGAM06-01 core site, during PNRA-ANARE WEGA expedition in 2000 (Brancolini, Harris and Shipboard Party, 2000).

Core U1361-1A-1H (length 9.05 m) is located at a depth of 3466 m at the Jussieu channel levee, downslope from the core WEGA PC20 site. The core was obtained with an Advanced Piston Coring (APC) system during the Integrated Ocean Drilling Program (IODP) Expedition 318 in 2010 (Escutia et al., 2011).

Core MD03-2603 (length 30 m) was recovered at 3290 m water depth on the internal side of the Cuvier canyon during the IMAGES-X CADO expedition (Michel and Crosta, 2003). This core is located at about 450 km west of the area where the other three cores were collected.

Sites MOGAM06-01, WEGA PC20 and U1361form a downslope transect from the continental slope (MOGAM06-01) to the lowermost part of the continental rise (U1361). These cores contain the depositional record of sediments delivered to the channel levee system from the George V Basin over the past 700 ka. Site MD03-2603 is located further to the west on the distal area of a levee mound located east of the Cuvier channel (Fig. 1). This site represents a “downstream” site with respect to site U1361, as it is influenced by the same along-slope bottom current (Escutia et al., 2002) but differs on the downslope source of terrigenous sediments that are delivered from the Dumont D'Urville Trough, on the continental shelf.

The cores collected in the study area are generally characterised by alternations of brownish to light yellowish brown diatom-bearing silty clays, and greenish-grey muddy sediments (Figs. 2, 3, 4 and 5; see also Caburlotto et al., 2009; Escutia et al., 2003 and 2011; Presti et al., 2011 for cores WEGA PC20, U1361A-1H and MD03-2603). Greenish-grey intervals are pervasively bioturbated as evinced by a mottled appearance, although discontinuous silt and clay laminations and layers

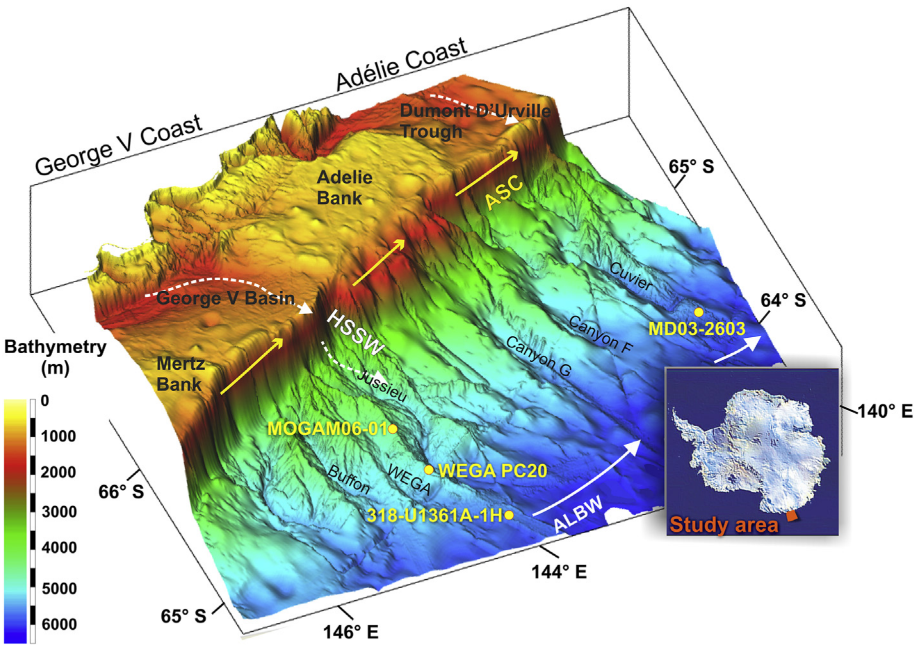

Fig. 1. Bathymetric map of the George V and Adélie Land continental margin, performed by Kingdom Suite ™ (IHS Educational Science), showing topography of shelf, slope and rise, main canyons crossing the area and illustrating the location of core sites. The map is viewed south-westward, to show the morphological setting of the margin. Swath-bathymetry data along the Jussieu, WEGA and Buffon canyons acquired during the PNRA-MOGAM cruise, 2006. Processed data kindly provided by Dr. R.J. Beaman (James Cook University, Australia; available at http://www.deepreef.org). Water masses: Adélie Land Bottom Water (ALBW), High Salinity Shelf Water (HSSW), Antarctic Slope Current (ASC). Inset map: Antarctica, evidencing the study area. The white dashed arrows show the schematic pathway of the HSSW forming on the continental shelf and flowing downslope.

locally occur, as well as local concentration of coarse terrigenous sand and gravel, interpreted as IRD. The laminated mud is characterised by packages of mm- to cm-scale silt and fine sand laminations, variable bioturbation and mm-size silt lenses.

3.2. Chronostratigraphic analyses and analytical procedures

Core MOGAM06-01 age model, is partially based on a single AMS ^{14}C date on bulk organic carbon, made on a 5-g-sample obtained at 23 cm depth in the core, measured at NOSAMS, Woods Hole Oceanographic Institute (lab code 88944). Preliminary biostratigraphic constraints were provided by smear-slide analyses of the diatom content on 25 samples collected between 5 and 385 cm. High-resolution paleomagnetic measurements were performed at 1-cm resolution on U-channel samples obtained from the MOGAM06-01 archive-half core. Measurements were conducted at the Paleomagnetic Laboratory of the Istituto Nazionale di Geofisica e Vulcanologia (Rome, Italy), using a "2G Enterprises" DC 755 superconducting rock magnetometer system installed in a magnetically shielded room. The natural remnant magnetization (NRM) of the sedimentary sequence was measured and then subjected to stepwise alternating field (AF) demagnetisation with peak fields of 10, 20, 30, 40, 50, 60, 80, 100 and 120 mT, with the aim to isolate the characteristic component (ChRM). Additional measurements were carried out to obtain the magnetic susceptibility (k) and the anhysteretic remanent magnetization (ARM), imparted in a 0.1 mT bias field combined with a peak AF of 100 mT and then AF demagnetized in 9 steps until peak field of 100 mT.

Core WEGA PC20 age model and palaeo-environmental magnetism were already studied by Busetti et al. (2003), Macrì et al. (2005), Damiani et al. (2006) and Caburlotto et al. (2009).

Site U1361 sediment characteristics and age model, based on biostratigraphic and paleomagnetic analyses, have been previously described by Escutia et al. (2011).

Sediment characteristics and age model of core MD03-2603 have been previously described by Presti et al. (2011). Here, we make use for the first time of absolute abundances of specific elements.

3.3. Geochemical analyses

Continuous downcore XRF were performed at 1-cm resolution on split sediment cores MOGAM06-01 and WEGA PC20 using an Avaatech XRF Core Scanner at the AWI in Bremerhaven. Tube voltage was adjusted to 50 kV, 30 kV and 10 kV in order to provide an optimum setting for several chemical elements. Details about the instrument and procedures are reported in Richter et al. (2006). The first core was analysed in 2009 with an Amptek XR-100CR (Si-PIN) and the second in 2011 with a Canberra X-PIPS SXD15C-150-500 (SDD) detector. XRF core-scanner analyses on sediment core U1361A-1H were performed at

Table 1
Core summary, type of investigation applied, and analyses performed here or within previous studies.

Project	WEGA	MOGAM	CADO	IODP, Leg 318
Core	PC 20	MOGAM06-01	MD03-2603	U1361A-1H
Longitude	143°55.9′ E	143°42.15′ E	139°22.51' E	143°53.20′ E
Latitude	64°54.09' S	65°17.20' S	64°17.12' S	64°24.57′ S
Water depth (m)	3014	2600	3290	3466
Core documentation	Brancolini, Harris and Shipboard Party, 2000	Boehm and Expedition Scientists, XXI PNRA expedition, 2006	Michel and Crosta, 2003.	Escutia, Brinkhuis, Klaus and the Expedition 318 Scientists, 2011
Core/Section length (cm)	463	400	3033	903
Grain size analyses	Caburlotto et al., 2009	*This study*	-	-
XRF Scan analyses	*This study*	*This study*	-	*This study*
ICP-AES analyses	-	*This study*	Presti et al., 2011 and *this study*	-
Age model	Macrì et al., 2005	*This study*	Presti et al., 2011	Escutia, Brinkhuis, Klaus and the Expedition 318 Scientists, 2011

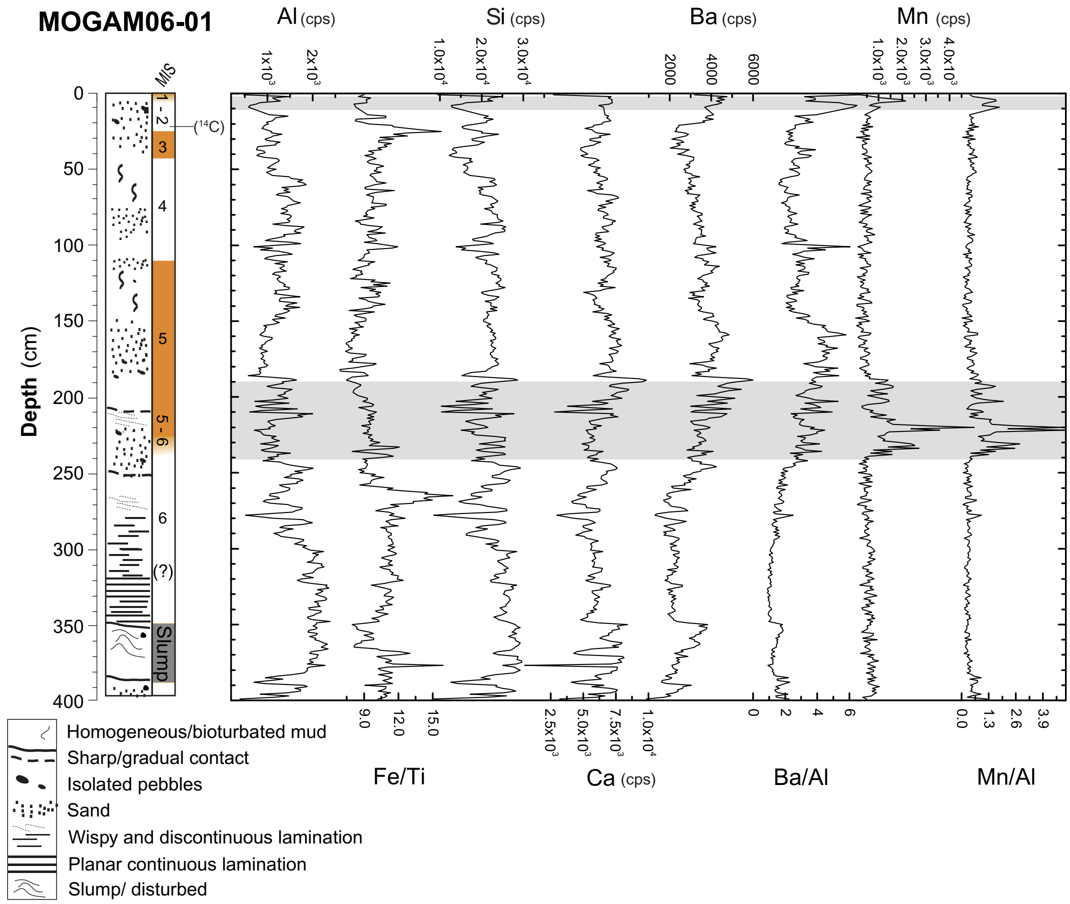

Fig. 2. MOGAM06-01 core log showing major sediment composition and structural features; chronology on the basis of RPI. Depth of the sample analysed for ^{14}C also shown. Down-core XRF-scan data (peak area counts per second = cps, plots in black, upper horizontal axis). Profiles of elements from XRF-scan are ordered according to their major affinity to lithogenous fractions (Al, Si, K, Ti, Fe), or else biogenous fractions (Ca, Ba). Mn is not related to these groups. Light-gray horizontal band at 190-240 cm: core interval with higher Mn abundance.

5-cm resolution by an Avaatech XRF Core Scanner at the IODP core repository in College Station (Texas, USA). We used a generator setting of 10 kV, with down-core slit size of 10 mm. For all XRF Core Scanner measurements the split core surface was covered with a 4 micron thin SPEXCerti Prep Ultralenel foil to avoid contamination of the XRF measurement unit and desiccation of the sediment. The basic unit of the XRF core scanner measurements is total counts or counts per second (cps), which is proportional to the real chemical concentration of the measured element (Tjallingii et al., 2007; Weltje and Tjallingii, 2008).

The analyses of major and minor elements by Atomic Emission Spectrometry were performed on 386 samples, collected at every 4 to 8 cm on core MD03-2603, and on 16 samples (every 20–30 cm) from core MOGAM06-01 for comparison with the XRF-core scanner data. The standard procedure indicated by McLaren et al. (1981) comprises: ground, homogenised, and sieved samples, were digested by ultrapure HF and HCl:HNO3 (3:1) into a DG Prep digestor (SCP Science). The solution obtained was analysed for its elemental content by ICP-AES IRIS Intrepid II XSP (Thermo Electron Corp.), according to the analytical procedure reported by Presti et al. (2011). Standard errors (σ) are below 2% for Al, Fe, Ti, below 5% for Ba, Mn and Ti, and below 10% for Mo. We report the data as absolute concentration in bulk sediments (mg/kg). The newly acquired data have been compared and related to the previously published analyses on the sediment record (Tables 2 and 3). To compare trace-element proportions in samples with variable carbonate and opal contents, it is common to normalize the absolute trace-element concentrations to Al or Ti, which are proxies of the aluminosilicate fraction of the sediments (Brumsack, 1989; Calvert and Pedersen, 1993; Morford and Emerson, 1999; Piper and Perkins, 2004) despite drawbacks that can occur with normalization (van der Weijden, 2002). Both Al and Ti normalizations have been already used in Presti et al. (2011) in core MD03-2603 and at all site locations, normalization by Al or Ti obtains identical patterns.

The data from XRF scan analyses (1251 samples) and ICP-AES analyses (402 samples) were examined statistically to describe the principal zones within the trace element abundances (absolute and relative) using the PAST 2.11 statistical software (Hammer et al., 2001; Hammer and Harper, 2006). A matrix is presented in both cases (Tables 2 and 3), with the correlation between all pairs of columns (variables) given as parametric coefficients (Pearson's r). Different variables are normalised to mean and standard deviation for each core analysed by XRF scan. For this paper, we used the elements analysed in all cores, i.e. 8 variables for XRF scan data (Al, Si, K, Ca, Ti, Mn, Fe and Ba), and 7 variables for ICP-AES analyses (Al, Ca, Ti, Mn, Mo, Fe and Ba). Principal component analysis (PCA) was also performed on the XRF scan data array combining all cores (Table 4), to assess the relative importance of each element in the extracted axis (variable loadings) and to calculate the strength of each axis in explaining the variance of a sample (case scores) (Monien et al., 2012 and references therein). The new variables (extracted axes) are linear combinations of the original variables. The hypothesis is that the most important components are correlated with other underlying variables.

3.4. Geochemical proxies in an Antarctic context

Manganese is one of the most reactive metals, which limits its utility as a redox proxy (Canfield et al., 1993). Difference in solubility of Mn

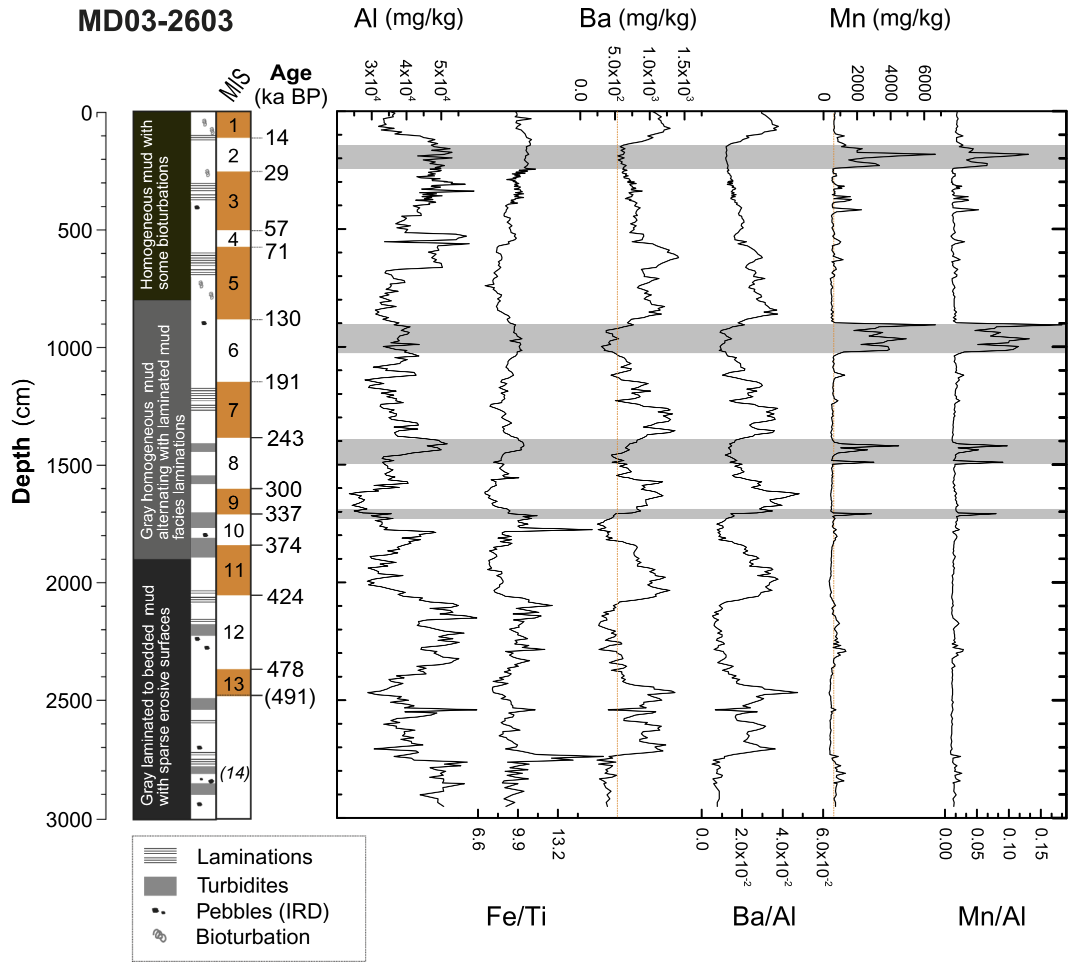

Fig. 3. MD03-2603 core log: major sediment composition, structural features and chronology. Down-core position of MIS boundaries are reported on the right of the descriptive log (Presti et al., 2011). Down-core ICP-AES data are ordered according to their major affinity to lithogenous fractions (Al, Ti, Fe), or else biogenous fractions (Ba, Ba/Al) and redox-change relation (Mn, Mn/Al). Dashed horizontal bands indicate Mn spikes corresponding to glacial /interglacial transitions (see text for discussion).

(II) and Mn (IV) species and reductive dissolution of oxyhydroxide particles may diffuse soluble Mn upward and downward within the sediment (Brumsack, 1989; Tribovillard et al., 2006 and reference therein). Mn in bulk sediment can be related to redox fronts and can react and shift after deposition. The redox gradation depends on the availability of oxygen and hydrogen sulphide (Froelich et al., 1979), and trace elements are involved in these reactions at various stages. Among them, Mn-oxides are solid phase electron acceptors that typically reflect past redox conditions in different environments (e.g., Calvert and Pedersen, 1993; Davison et al., 1982; Eusterhues et al., 2005; Löwemark et al., 2008). Typically, the distribution and precipitation of Mn in bottom waters is mainly controlled by oxygen conditions (Yarincik et al., 2000). A change in redox conditions would lead to a change of dissolved manganese (Mn^{2+}) content of the water column and/or pore-water, and would result in consequent precipitation of Mn (Pakhomova et al., 2007). Nevertheless, with some cautions, Mn is useful for identifying deep-water ventilation changes in the Southern Ocean (e.g., Jaccard et al., 2016) and other marine basins (e.g., Mangini et al., 2001; Jimenez-Espejo et al., 2007; Kaboth-Bahr et al., 2018). To avoid interpreting local or spurious Mn peaks, we performed a multisite study in order to interpret only Mn enrichment with regional significance. We also compensate some of the weaknesses of Mn single element application by coupling its down-core with other redox (e.g, Mo), detrital (e.g., Al, Ti, K) and biogenic (e.g., Ca, Ba) proxy record and sedimentology.

Barium has been commonly used as a "paleoproductivity proxy" in Antarctic sediments (e.g. Hillenbrand et al., 2009; Escutia et al., 2009), but it should be applied with some caution in contourite systems (Bahr et al., 2014). At the studied locations, we can ascribe the high content in Ba and Ca content to a reduced strength/frequency of the terrigenous input associated to mass transport processes (minimum in Al, Fe and Ti) during periods of reduced marine-based ice sheet advance (interglacial stages), characterized by reduced delivery of sediment to the continental shelf edge. In addition, the minor terrigenous input may be associated to an increase in marine productivity related to environmental amelioration or enhanced preservation of biogenic particles (mainly diatoms) during interglacials.

Al and Ti are found mainly in aluminosilicates, sediment coarse fractions, and heavy minerals that are not significantly involved in biological or redox process (Calvert and Pedersen, 2007); allowing the use of these elements as detrital proxies (e.g., Rodrigo-Gámiz et al., 2014). At the Wilkes Land margin, it has been observed that erosion in different bedrock types produced variable mineralogical composition and grain sizes during different glacial/interglacial periods (Cook et al., 2017). In detail, the K/Ti ratio appears to be a robust proxy for reconstructing the provenance of terrigenous material and is very sensitive to glacial/interglacial oscillations because AL-GVL feature lithology (Bertram et al., 2018).

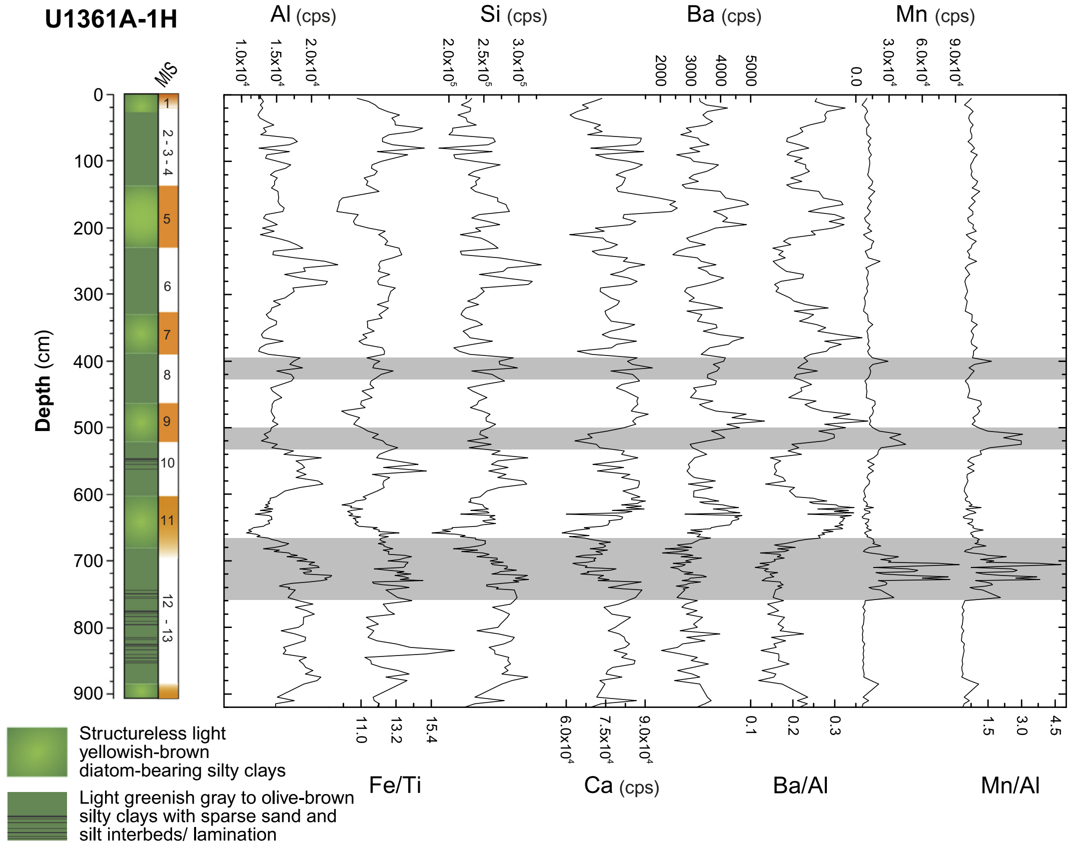

Fig. 4. U1361A-1H core log showing major sediment composition and structural features, on the basis of Escutia et al. (2011) and XRF-scan data (this paper). Down-core positions of diatom-bearing intervals (Escutia et al., 2011), interpreted as deposited during interglacial periods (MIS 3, 5, 7, 9, 11 in particular), are reported on the right of the descriptive log and are further used to infer the position of interglacial/glacial stages in Fig. 7. Light-gray horizontal bands: peaks of Mn at the transition from glacial to interglacial sediment intervals.

4. Results

4.1. Age models

The age models of cores WEGA PC20, U1361A-1H and MD03-2603 have been presented previously by Macrì et al. (2005), Caburlotto et al. (2009), Escutia et al. (2011), and Presti et al. (2011). The age model of core WEGA PC20 was developed from high-resolution paleomagnetic and biostratigraphic data (Macrì et al., 2005; Caburlotto et al., 2009). The core reaches ~470,000 years before present (470 ka BP) to Marine Isotope Stage 19 (MIS 19) and exhibits a mean sedimentation rate of ca. 1 cm/ka. Biostratigraphic and paleomagnetic data from site U1361A indicate that the base of core U1361A-1H likely dates about 500 ka BP, based on an estimated sedimentation rate of ca. 1.8 cm/ka during the Mid to Late Pleistocene according to Tauxe et al. (2012), and Patterson et al. (2014). Concerning core MD03-2603, Ba/Al and Ba/Ti ratios demonstrated a high coherence with glacial-interglacial cycles observed in the LR04 $\delta^{18}O$ benthic stack (Presti et al., 2011) and allowed to date the base of the core at ~500 ka BP, with an estimated sedimentation rate of ca. 6 cm/ka.

An original age model, based on palaeomagnetic measurements, is compiled in this paper for core MOGAM06-01 (Fig. 6). Relative Paleointensity (RPI) curves of the geomagnetic field derived by comparison with the existing global reference curves (e.g. SINT-800 of Guyodo and Valet, 1999; PISO-1500 of Channell et al., 2009) and regional reference RPI SEDANO and WEGA stacks (e.g. Macrì et al., 2005, 2006). In particular the RPI records of core MOGAM06-01, obtained with the different parameters of normalization (NRM_{20mT}/k and NRM_{20mT}/ARM_{20mT}) show a similar pattern, supporting evidence for a general coherency between the normalisation procedures (Fig. 6, upper box). RPI curves do not agree very well in some case because lithology of the sediment core is not uniform. For this reason, we decide to first correlate the MOGAM06-01 core with the already dated WEGA PC20 core using the available different magnetic parameters. Moreover they can be correlated by means of the main features of the geomagnetic field recorded by the sediments and the relative positions of the geomagnetic excursions and events already globally known in that time interval (see Laj and Channell, 2007 for review). Assignment of ages from the dated reference curves to the individual RPI records of core MOGAM06-01 (e.g. paleointensity highs at 25-30 cm, 255 cm and from 315-340 cm and the lows around 50 cm, 100 cm, 250 cm and 350 cm; Fig. 3), identifies the positions of the MIS 2/3 boundary at around 26-28 cm, MIS 3/4 boundary at around 42-43 cm and MIS 4/5 boundary between 88-110 cm. Radiometric AMS ^{14}C dating on the bulk organic carbon of a sample located at 23 cm depth gives an uncorrected age of 28200 ± 230 a BP, which is likely an estimated maximum age for the sample analysed, due to reworking, and old finite carbon particles in the sediment.

Biostratigraphic analyses were conducted on the diatom content in 25 smear-slide samples distributed throughout core MOGAM06-01 show that the diatom *taxa*, representing the biosiliceous content in this core, are modern Antarctic sea ice and Southern Ocean endemic forms (e.g. *Fragilariopsis kerguelensis*, *Chaetoceros* resting spores, *F. obliquecostata* and *Eucampia antarctica* var. *recta*). These are commonly found in late Pleistocene-Holocene sediments and are useful in biostratigraphic and paleoenvironmental reconstructions (Escutia et al., 2003; Armand et al., 2005; Crosta et al., 2005; Macrì et al., 2005; Caburlotto et al., 2009; Presti et al., 2011; Tolotti et al., 2017). *Rouxia leventerae*, whose last occurrence datum is used to infer the MIS 5/6 boundary (Zielinski and Gersonde, 2002), was found at the bottom of

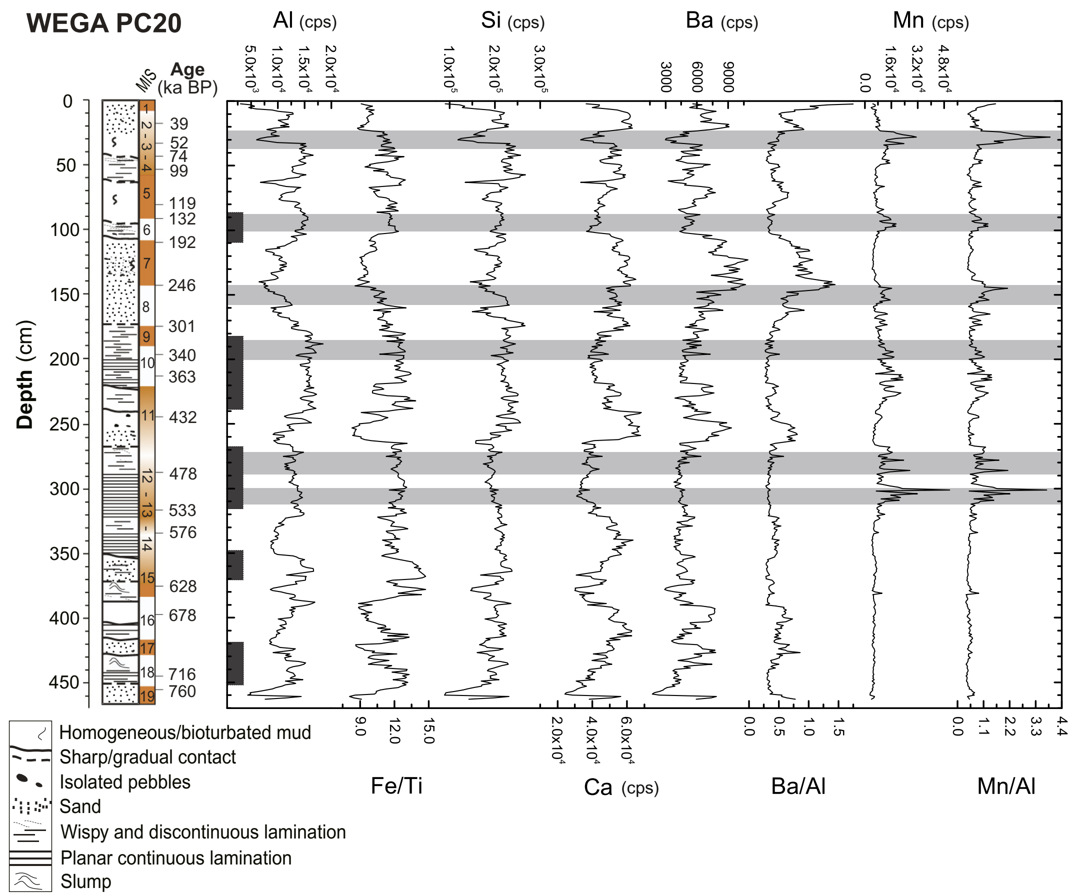

Fig. 5. WEGA PC20 core log showing major sediment composition and structural features. Down-core position of tie-points and position of corresponding Marine Isotopic Stages (MIS) from (Macrì et al., 2005). Major sediment composition and XRF-scan data, as for Fig. 3. Light-gray horizontal bands: peaks of Mn, at the transition from glacial to interglacial sediment intervals. Dark-gray horizontal bands: turbidites and slumps.

the core up to 240 cm. These data allow to us estimated sedimentation rate of ca. 1.4 cm/ka for the upper 350 cm.

4.2. Geochemical analyses

X-ray fluorescence scan analyses were performed on cores WEGA PC20, MOGAM06-01 and U1361A-1H. All datasets show similar down-core trends for two sets of elements that are significantly correlated together: 1) Al, Si, K, Ti, Fe, and 2) Ba and Ca (Table 2). The down-core distribution of Al, Si, K, Ti, and Fe show high values during glacial periods (Figs. 2-5). The record of Ca and Ba displays antiphase oscillations with respect to the previous group of elements. The downcore variations of Mn varies between cores (Fig. 7), but, all cores display distinct "spikes" of this element above background values that commonly occur near glacial terminations. The magnitude of these spikes varies between cores (Fig. 7).

The correlation for ICP-AES analyses (Table 3) is significant for groups of elements showing a broadly similar down-core trend, as follows: Al, Fe, Ti, are well correlated together, Mn matches with Mo, Ba, and it is negatively correlated with most of the former elements.

In terms of down-core profiles that show the same co-varying oscillations (Fig. 2), the down-core trend of the abundance of the elements analysed in core MOGAM06-01 can be compared to 1-cm-resolution XRF scan data described above. Mn abundance in core

Table 2
XRF-scan analyses data on cores WEGA PC20, MOGAM06-01 and U1361: Pearson's correlation coefficients, reported in the bottom left triangle and significance *p*-values reported in the top right triangle. Variables (elemental peak area cps) have been standardized for each core to their mean and standard deviation. In order to determine the required level of confidence ($\alpha_{required}$), we used the Šidàk-Bonferroni correction, according to Abdi (2007): $\alpha_{required} = 1 - (1 - p)^{1/n}$. If the associated probability of the test (p value) is smaller than the required level of confidence α, then the test is significant. At $p < 0.0001$, for 1251 samples (n), $\alpha_{required}$ is $< 7.99 \times 10^{-8}$. Bold fonts for coefficients represent significant values, since the associated probability is lower than $\alpha_{required}$. Underlined fonts for coefficients represent moderate or strong positive or negative correlation. Note high correlation between Si, Al, Fe and Ti; also, Mn behaviour is not related to that of any other element.

	Al	Si	K	Ca	Ti	Mn	Fe	Ba
Al		0	0	*5.7E-07*	0	*1.9E-07*	0	2.1E-13
Si	**0.838**		3.1E-262	1.9E-68	1.2E-205	*0.012*	4.3E-114	*0.002205*
K	**0.947**	**0.736**		*0.039*	0	*1.3E-07*	0	3.4E-26
Ca	0.127	**0.425**	0.053		4.2E-13	*0.0002*	6.5E-13	7.7E-41
Ti	**0.820**	**0.676**	**0.805**	**0.184**		*0.192*	4.8E-282	*0.008*
Mn	0.132	*0.064*	0.134	*-0.096*	*0.033*		*3.3E-08*	*0.0003*
Fe	**0.798**	**0.534**	**0.857**	**-0.182**	**0.754**	0.140		2.3E-55
Ba	**-0.186**	*0.078*	**-0.266**	**0.332**	*0.068*	*-0.093*	**-0.385**	

Table 3
ICP-AES analyses data on cores MD03-2603 and MOGAM06-01: Pearson's correlation coefficients, reported in the bottom left triangle and significance values p reported in the top right triangle. Bold fonts for coefficients represent significant values with $p < 0.0001$. Underlined fonts for coefficients represent moderate (> 0.5) or strong (> 0.7) positive or negative correlation. In order to determine the required level of confidence ($\alpha_{required}$), we used the Šidàk-Bonferroni correction. At $p < 0.0001$, for 402 samples (n), $\alpha_{required}$ is < 2.49 x 10^{-7}. Note the correlation between Mn and Mo.

	Al	Ba	Ca	Fe	Mn	Mo	Ti
Al		3.0E-13	0.592	1.6E-36	0.007	0.134	7.7E-09
Ba	**-0.353**		0.030	4.0E-49	3.5E-08	0.248	1.8E-16
Ca	-0.027	0.109		6.5E-03	0.003	0.071	5.9E-02
Fe	**0.573**	**-0.647**	0.136		3.0E-08	0.010	3.3E-42
Mn	0.134	**-0.271**	0.148	**0.272**		0	2.8E-02
Mo	0.075	-0.058	0.090	0.128	**0.597**		7.7E-01
Ti	**0.283**	**-0.395**	0.094	**0.609**	0.109	0.014	

Table 4
Principal Component Analysis of integrated XRF-scan data: variable loadings for the three significant Axes. Bold fonts: highest load of each variable in the corresponding Axis. Mn is significant only for Axis 3. Variance explained: Axis 1 = 51.09%; Axis 2 = 22.99%; Axis 3 = 12%.

PCA variable Loadings	Axis 1	Axis 2	Axis 3
Al	**0.442**	0.108	0.050
Si	**0.362**	0.232	-0.121
K	**0.441**	0.040	0.104
Ca	0.037	**0.502**	-0.423
Ti	**0.374**	0.270	0.143
Mn	0.061	-0.073	**0.584**
Fe	**0.394**	-0.073	0.308
Ba	-0.141	**0.555**	-0.026

MOGAM06-01 is higher than the reference shale for the interval corresponding to the likely transition from MIS 6 to MIS 5, and is defined by a distinctive double spike (Figs. 2 and 7).

4.3. Statistical analyses

PCA on the elemental X-ray fluorescence scan data, combined in a single array of samples ($n = 1251$), for each variable and each core (Table 4) has been conducted to better discriminate geochemical variations and associated sedimentary process, provenance changes and climate variations (Fig. 8), using the PAST 2.11 statistical software. Data standardization was performed before PCA because: (1) the differences in water content among the cores are likely to affect the relative measurement of lighter elements, such as Al and Si (Richter et al., 2006; Weltje and Tjallingii, 2008); (2) the cores were scanned by different detectors with, possibly, different sensitivity. The calculated eigenvalues (Table 4) give a measure of the variance accounted for by the corresponding components (*axes* of the PCA). The first three axes, yielding eigenvalues > 1 (significant components with values higher that the *Jolliffe cut-off*; Jolliffe, 1986), illustrate the most significant transitions and the elements that characterise these changes.

The first 3 axes of the PCA yield respectively percentages of variance of 51.1%, 22.9%, 12%, accounting for 86.8% of the total variability in the major and minor elements down-core distribution. The main positive loadings for PC1 for all combined cores are Al, K, Ti and Si (Fig. 8a). The main positive loadings for the PC2 are Ba, Ca and Si, as well as negative loadings for Fe, Al and K. The main loadings in PC3 at the studied sites are Ca, Si and Al (positive) and Mn (negative) (Fig. 8a).

In order to better identify biogenic, terrigenous and diagenetic increase of specific elements, a record of the absolute concentrations of Al, Ba, Fe and Mn were produced via ICP-AES analyses on discrete samples for cores MD03-2603 (386 samples; Fig. 3). We report the absolute abundance of each trace element, together with its average upper crust content (McLennan, 2001) shown as reference (Fig. 3). We selected McLennan (2001) because showed the lowest values in comparison to previously published global datasets, aiming to minimize the contribution of diagenetic enrichment of a certain trace element to the average crustal abundance. For core MD03-2603 (Fig. 3) the range of concentrations for all elements is similar to that of core MOGAM06-01. The Mn record is characterized by a variability of one order of magnitude, with values close to zero during interglacials and high spikes mainly corresponding to the uppermost part of glacial intervals, and likely associated to glacial terminations (deglaciation).

5. Discussion

5.1. Geochemical variations as proxy for glacial versus interglacial deposition

The application of the PCA case score plots and loadings helped to distinguish multivariate elemental changes relating to different depositional conditions (Fig. 8a). Axis 1 is consistent with variations in the lithogenic, aluminosilicate fraction (Al, Si, K, Ti, Fe). Axis 2 represents the elements related to the biogenic fraction (Ca, Ba, and low loadings of Si). Axis 3 includes the elements related to diagenetic processes (Mn). High Si-load on both axes is explained by the Si contained in both terrigenous aluminosilicates (clays) and siliceous microfossils such as diatom frustules that form the main biogenic silica component. The correlations between Ca, Si and Ti can be explained by a part of the Ca pool is included into aluminosilicates, and by the presence of detrital calcite. The high correlation observed between Ca and Ba suggests that both elements are controlled by the same process, i.e. more/less concentration of the biogenic fraction diluted into the terrigenous fraction.

Glacial sediments are dominated by lithogenic elements (Axis 1) (Fig. 8b) and high Fe/Ti ratio (Figs. 2-5), whilst interglacial sediments are characterised by an increase in biogenic inputs (Axis 2), with some differences between cores. For instance, at site WEGA PC20, the Ba trend failed to provide a clear variability of the sediments composition between glacial and interglacial intervals between 780 ka BP to 530 ka BP. The older part of the core contains a disturbed glacial/interglacial interval attributed to post depositional deformation (Fig. 5), and/or a chaotic input of coarse terrigenous fractions. This characteristic has been related elsewhere to frequent proximal density currents and sediment failures along the continental slope during glacial periods (Lucchi et al., 2002; Lucchi and Rebesco, 2007).

Cores WEGA PC 20, U1361A and MD03-2603 (Figs. 3-5) record the Mid-Brunhes Event (MBE, 430 ka BP), which roughly corresponds to the transition between MIS 12 and MIS 11 (Termination V). Pre-MBE sediment units record turbidite sequences with a low post-depositional reworking at site WEGA PC 20 and MD03-2603, while productivity proxies show no distinctive peaks during MIS 13 at core U1361A. The lack of bioturbation, flat Mn-based record (Fig. 7) and absence or poor preservation of biogenic barite during pre-MBE intervals (MIS 13 and older) can be explained by permanent low oxygen conditions and low marine productivity at this location. These conditions can be explained by reduced oxygenation (and likely formation) of AABW during pre-MBE interglacial periods in comparison to post-MBE interglacials, potentially due to lack of coastal polynyas on the shelf due to ice sheet expansion toward the shelf edge. This evidence fit with the reconstructions from Prydz Bay (Leg 188), Ross Sea (ANDRILL), and the Antarctic Peninsula (Leg 178), where the pre-MBE ice sheet advance across the continental shelves was extensive, while the ice sheet retreat during interglacial periods was minor (Cooper et al., 2004; Hepp et al., 2006). The strength of the Antarctic Circumpolar Current probably was probably dampened, due to less wind shear linked with a northward displacement of the wind fields and sea-ice edge. These observations are in agreement with recent studies that described pre-MIS 11 interglacial periods as attenuated or "lukewarm" interglacials (EPICA

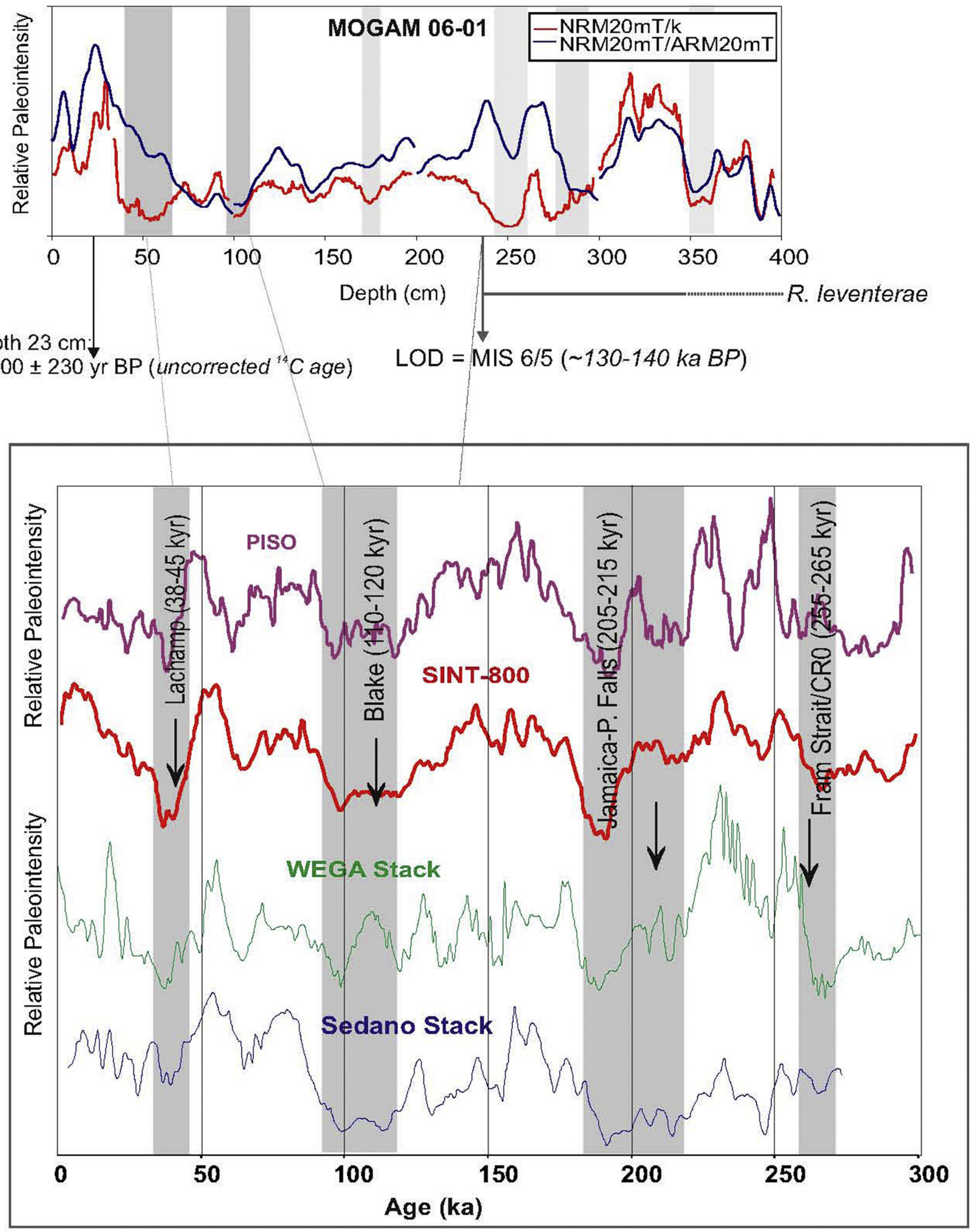

Fig. 6. RPI records of the MOGAM06-01 obtained with the different parameters of normalization (NRM_{20mT}/k and NRM_{20mT}/ARM_{20mT}) compared with the existing global reference curves (PISO-1500 of Channell et al., 2009; SINT-800 of Guyodo and Valet, 1999) and regional reference RPI stacks (WEGA and SEDANO stacks of Macrì et al., 2005, 2006). Position and ages of the main globally recognised geomagnetic events and excursions were reported with black arrows positioned within grey vertical areas, corresponding to the main RPI minima and compared with the biostratigraphic interpretation based on Zielinski and Gersonde, 2002.

community members, 2004; Jaccard et al., 2013), and an increase in the amplitude of glacial–interglacial climatic cycles after the MBE (e.g., Lisiecki and Raymo, 2005; Jouzel et al., 2007; Yin and Berger, 2010). Similar conditions have been also recorded in the Northern Hemisphere where extreme stadial events and glacial/interglacial amplification are described after the MEB (e.g., Croning et al., 2017; Rodrigues et al., 2017). To summarise, we infer that the source region of AABW must have shifted offshore during pre-MBE periods, into deeper water. Consequently, reduced overturning and ventilation of the abyssal Southern Ocean, along with reduced changes over glacial-interglacial timescale, could explain the lower amplitude variations and overall concentrations of CO_2 observed in ice cores during this time period relative to post-MBE interglacial-glacial cycles (Lüthi et al., 2008).

During post-MBE interglacial periods, higher bioturbation within cores MD03-2603; MOGAM06-01 and WEGA PC20 can be recognized (Figs. 2, 3 and 5). These reworking processes were probably enhanced by increased oxygenation of the sediment which favoured benthic organisms. Post-MBE glacial to interglacial periods are marked by large amplitude variations in the Ba/Al, Fe/Ti and Mn/Al ratios, especially at site U1361A-1H (Fig. 4). These observations might be explained by the presence of polynyas on the continental shelf during interglacial periods, likely enhancing the AABW formation, and higher ice-sheet variability during the late Pleistocene post-MBE glacial-interglacial cycles.

The MIS 6/MIS 5 transition, biostratigraphically confirmed by the diatomaceous *R. leventare* marker event, can be observed in detail in Figure 9 and the supplementary information reporting 3D X-ray Computed Tomography animations of core MOGAM06-01 (https://youtu.

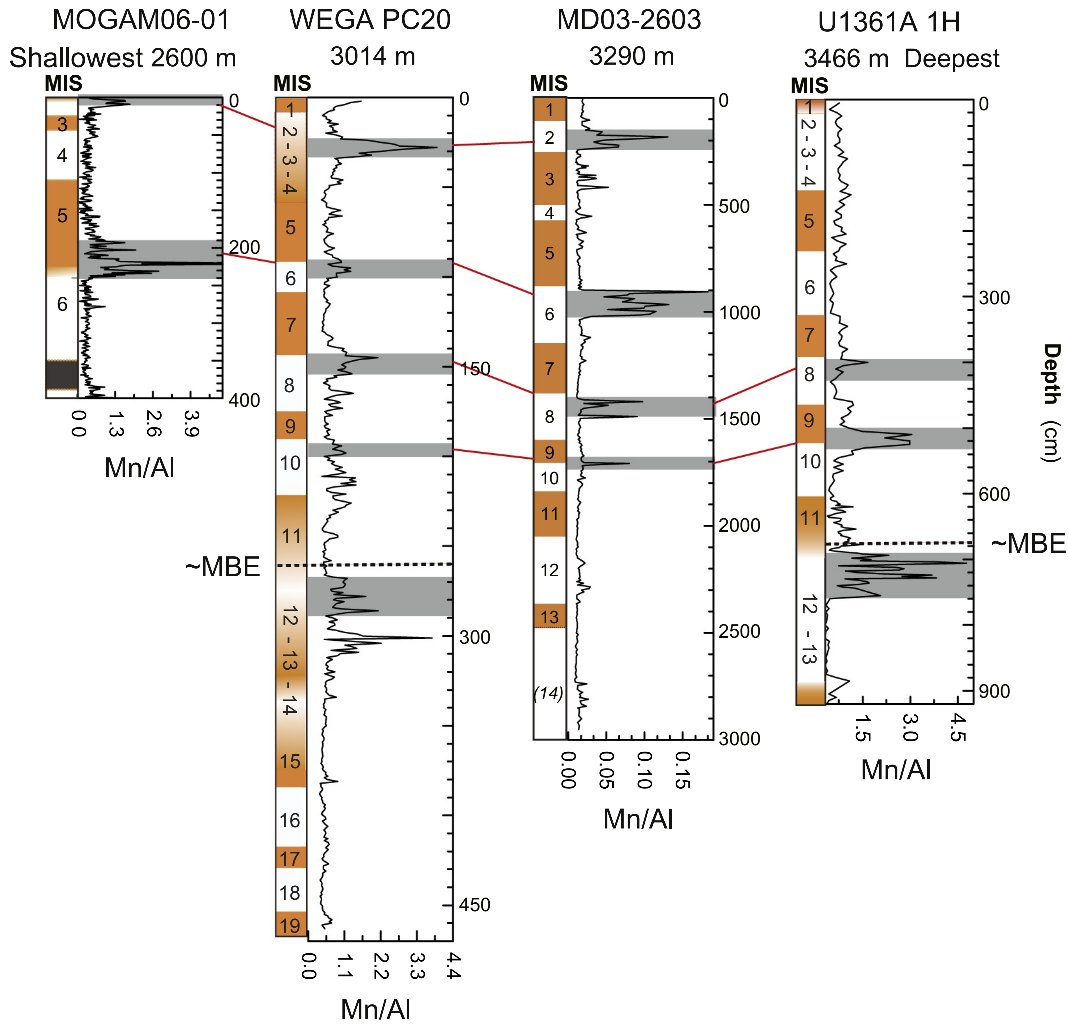

Fig. 7. Mn/Al ratio depth plotted comparison among cores. Grey bars at sites MOGAM06-01, WEGA PC20, MD03-2603 and U1361 represent Mn enrichments associated to glacial to interglacials transitions and Mn/Al ratio enrichments with "double peak" morphology. Vertical bar numbers represent marine isotopic stages (orange colour indicates interglacials). MBE: Mid-Bruhnes event (430 ka BP).

be/46HpallTMXU and https://youtu.be/fLkEdPsFcpk). These animations show an extensively-bioturbated interval (154-160 cm), within an interglacial period (likely MIS 5), and a transition from a lower IRD-rich interval to an upper bioturbated interval (230-240 cm), corresponding to the transition from a glacial to an interglacial period. After this transition, coarser turbidite layers and intervals of laminated silt/clay sediments during the glacial/interglacial transition become less common at sites MOGAM06-01; WEGA PC20 and MD03-2603, (in comparison to older transitions), because of the reduced input of lithogenous material from the shelf, previously massively delivered during glacial periods (Figs. 2, 3 and 5). Glacial/interglacial variability is less marked in all studied sites from MIS 5 to MIS 1 in productivity (Ba/Al ratio) and detrital (Fe/Ti ratio) proxies probably linked to this decrease in detrital input and minor variations in ice sheet until MIS 1.

5.2. Water masses evolution as detected by redox conditions

As mentioned in Section 3.4, Mn used as redox proxy should be applied with caution. In this study, Mn use as redox proxy relie on three considerations: i) In order to discard local Mn enrichments non-associate to major paleoenviromental changes, interpretations are only based in coetaneous variations obtained in at least two sites (Fig. 7) and significance compared with other proxies and regional studies. ii) The application of the PCA case score plots and loadings distinguish Mn from lithogenic and biogenic fractions (Table 4), pointing to a diagenetic origin (Fig. 8). iii) Mo is considered a robust redox proxy (e.g., Tribovillard et al., 2006) and Mn and Mo in the cores MD03-2603 and MOGAM06-01 display a significant correlation (Table 3).

The largest peaks of Mn in our cores sign in the sediments the transition from glacial to interglacial intervals (Fig. 7, light-gray horizontal bars) with characteristic down-core double peak in most cases. The glacial/interglacial transition is reflected also in the PCA as high component scores on axis 3 (Fig. 8b). A few, low-amplitude Mn enrichments appear in glacial periods, which are likely due to variations in grain size, pore water, and other lithological changes (e.g., Löwemark et al., 2008). Core WEGA PC20 site, records the largest sedimentary variations and shows a complex Mn down-core pattern. Nevertheless, the Mn peaks are clearly present in the glacial to interglacial transitions (Fig. 7, light-grey horizontal bars). At site MD03-2603, Mn enrichments appear to correspond with turbidite levels (Figs. 3 and 7, dark grey bars in the core log, on the left).

The formation of double Mn peaks (and described relation with other redox-sensitive elements) during transitions can be accounted by redox fronts promoted by better-ventilated deep water covering sediments that deposited under less ventilated conditions. Sudden sediment re-oxygenation led to hydrogenic deposition or precipitation of the upper Mn peaks (Van Santvoort et al., 1996; Thomson et al., 1995). These upper peaks are synchronous with ventilation changes and

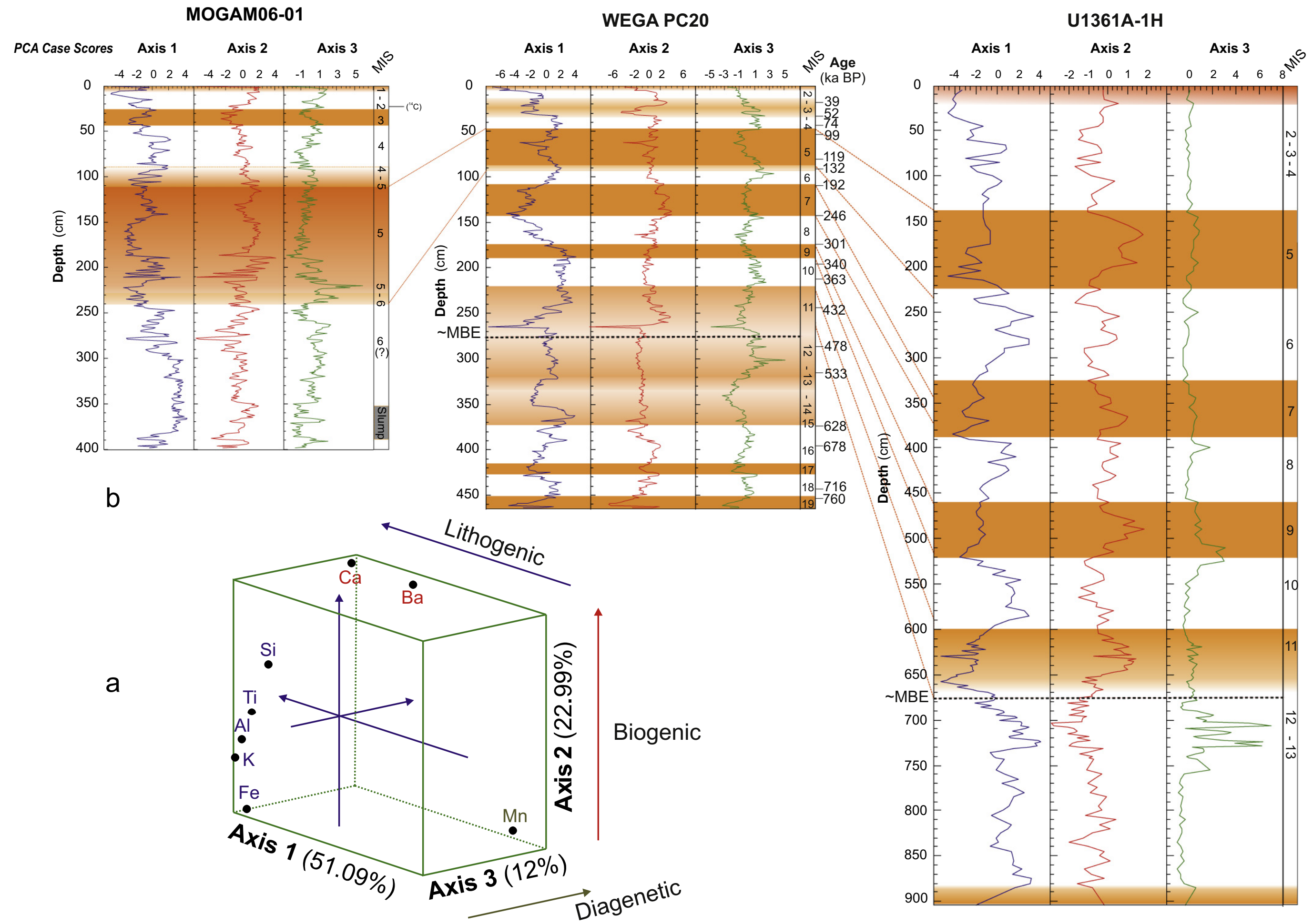

Fig. 8. a) Relationship among variable loadings for the first three axes of the Principal Component Analysis run on normalised data from XRF scan of cores MOGAM06-01, WEGA PC20, U1361A-1H, shown as a 3D-box plot. Al, Si, K, Ti, Fe have higher loadings on axis 1; Ba, Ca on axis 2; Mn on axis 3. **b)** Down-core plot of the first three axes of the PCA. Correlation among MIS of core MOGAM06-01 and WEGA PC20 is based on core chronologies as described in the text. A correlation between core WEGA PC20 and core U1361A-1H is reported. The sedimentation rate of core WEGA PC20 is lower than that of core U1361A-1H, despite the latter is more proximal to the continental margin, likely because core WEGA PC20 is located on the uppermost part of a mound/levee. Sediment units in core WEGA PC20 deposited during MIS 5, 7, 9, 11 (i.e. interglacial stages) have been related to sediment intervals in core U1361A-1H corresponding to diatom-bearing sediments (Fig. 5), considering that according to post-cruise biostratigraphic analyses the whole core section 1H is younger than 535 ka BP (Escutia et al., 2011). Diatom-bearing sediments yield also higher scores for axis 2 and lower for axis 1. Note the uncertainty in correlation for sediments older than MIS 11/12. MBE: Mid-Bruhnes event (430 ka BP).

outline key intervals for further water masses reconstruction studies (Mangini et al., 2001). The oxidation front began to penetrate downcore through the sediment column. This redox front blocked the upward diffusion of Mn^{2+}, forming the lower Mn enrichments (e.g. Rutten et al., 1999), controlled in turn by sedimentation rate and porosity (Jung et al., 1997). Similar Mn patterns have been found in different marine basins (Van Santvoort et al., 1996; De Lange, 1998; Mangini et al., 2001; Jimenez-Espejo et al., 2007), where they are interpreted as the penetration of a redox front. Oxidizing agent replenishment may be observed when environmental conditions vary (relatively) abruptly, such as glacial/interglacial transitions (Reitz et al., 2004; McManus et al., 2005). Thus, we propose that these glacial/interglacial redox events represent the transition from poorly ventilated glacial environments to highly ventilated environments. These changes can be explained by dense HSSW formation on the Wilkes Land margin and cascading phenomena that were intense enough to circulate saline and oxygenated waters through deep channels during or after ice sheet retreat. This evidence is also supported by the described sedimentological features, where poorly bioturbated turbidites (low oxygen conditions) alternate with well-ventilated reworked turbidites. Equivalent oxy-redox geochemical patterns have been observed in the Northern Pacific (Korff et al., 2016) and Arctic ocean, where episodes of high Mn enrichments are also a common feature within long cores (Löwemark et al., 2008) and interpreted, among others, as changes in oxygenated waters between glacial periods (Jakobsson et al., 2000; März et al., 2011), or in association with ice-sheet collapse during glacial terminations (Lucchi et al., 2013, 2015).

This implies that, after the Mid-Brunhes Event, the Wilkes Land margin contributed to the AABW formation mainly during interglacial and transitional periods in conditions similar to those reconstructed in Figure 10. These evidences are in agreement with AABW production rates in the Weddell Sea and other regions, when AABW production below shelf ice mainly forms during interglacial and early glacial periods, and production shuts down during Terminations and full glacial conditions (Krueger et al., 2012; Wagner and Henry, 2017). AABW production by brine rejection was mainly active during transitions from glacial to interglacials (Borchers et al., 2016). The reduction of deep water formation during full glacial conditions has been linked with a strong reduction of open polynyas on the shelf and displacement of sites of bottom water formation (Mackensen et al., 2001).

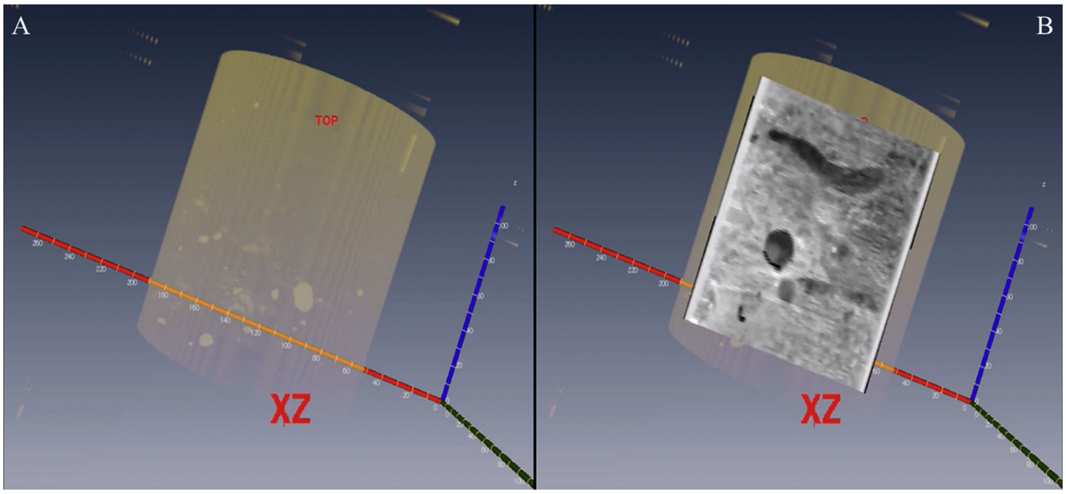

Fig. 9. Images captured from X-ray computed tomography animation of core MOGAM06-01 between 230-240 cm depth (X, Y and Z axis, white marks represent 1 cm). Selected interval represents MIS 6 (glacial) to MIS 5 (interglacial) transition. a) X-ray image where brightest colours represent high density grains (ice rafted debris) into a low density matrix (hemipelagic sediment). b) Selected computed tomography slice with grey scale (light colour = higher density; dark colour = lower density). Trace fossils and bioturbation appears as elongated and rounded forms, concentrated within the middle and upper core intervals.

A more complex down-core Mn trend appear during the MIS 5/6 when Mn/Al enrichments are clearly observed at MOGAM06-01 (2600 mbsl) and MD03-2603 (3290 mbsl) sites with minor evidences at the WEGA PC20 (3014 mbsl) and U1361A (3466 mbsl) sites. In addition, MOGAM06-01 Mn/Al enrichment occurs after the MIS 5/6 transition, but at MD03-2603 it appears to precede this period, showing that they are not synchronous, or there was anomalously high sedimentation rates at MOGAM06-01 site during the deglaciation (Lucchi et al., 2013, 2015). This result can be interpreted as a progressive shallowing of the redox boundary, and as associated abrupt fluctuations of water masses and chemical fluxes, from 3290 mbsl (MD03-2603) to 2600 msbl (MOGAM06-01) over few thousand years. Similar relationships can be seen during other periods (Fig. 7) but we cannot discard that proximity to the margin, different sedimentation rate, different glacial catchments feedings the heads of these two distinct canyon systems, and previous explained processes affecting preservation of Mn-enrichment could explain these differences among cores.

In any case the MOGAM06-01 record indicates that at least during MIS 6 low oxygen conditions existed at 2600 m of water depth, which extrapolated to the entire area, it would indicate a major expansion of poorly oxygenated water during this glacial period. These poorly oxygenated waters could accumulate heat, CO_2 and $Si(OH)_4$ during glacial periods, as describe during the Last Glacial Maximum (Anderson et al., 2009; Meckler et al., 2013; Ronge et al., 2015), that can reach the surface during convection onset and promote fast Antarctic warming at the glacial termination (Pedro et al., 2016). Data acquired at Wilkes Land margin indicate that deep poorly oxygenated waters were at least hundreds of meters shallower in the past, favouring their participation in convective heat phenomena during deglaciation when ice-shelf collapsed likely by exposure to Circumpolar Deep Water (Ritz et al., 2015). The reconstruction of bottom water low oxygen conditions in our study is also in agreement with studies that point to the Antarctic Zone of the Southern Ocean as an effective CO_2 trap/sink during glacial periods (Jaccard et al., 2016).

6. Conclusions

The Late Pleistocene oceanographic and depositional history of the channel-levee complex of the Wilkes Land continental margin is documented by several environmental proxies from a depth transect of four sediment cores.

The entire margin is affected by a progressive decrease in terrigenous supply of glacigenic origin provided to the shelf break-upper slope, and funnelled down-slope along the channels system during the last 500 ka. Lithogenic material dominated by terrigenous debris is characteristic of deposits older than the MBE (430 ka BP), that fails to clearly record a difference in glacial/interglacial deposition. A progressive increase in the glacial/interglacial variability in the sediment variability can be pointed out post MBE with a significant increase in biogenic elements (Ca, Si and most of all Ba) that clearly marks the interglacial deposition. The biosiliceous content, characterized by specific and endemic Pleistocene-Holocene taxa, has proved to be a valid and promising support for paleoceanographic and ages determination.

The Mn inventory of all cores shows common enrichments at the transitions between glacial to interglacial intervals interpreted as the variation from poorly oxygenated waters during glacial conditions, to well oxygenated waters at glacial-interglacial transitions, when the mechanism of HSSW formation is switched on. Mn content in the downslope transect of cores allowed us to reconstruct that low oxygen conditions during MIS 6 reached at least reached 2600 m water depth in this margin. Comparison of the obtained data with other Southern Hemisphere basins indicates a substantial shutdown of the modern mode of AABW formation during glacial periods (Wagner and Henry, 2017), in agreement with studies that point to a decrease in shelf water formation (e.g. Mackensen et al., 2001; Krueger et al., 2012), and abrupt formation of oxygenated, dense shelf water masses during early interglacial periods. Further studies would be necessary to find analogies of conditions along the margin during the deglaciation, and the recent break-up episodes of the ice shelf in some areas, relevant to the present freshening of ocean water masses of the continental shelf and deep waters in this region (Aoki et al., 2013).

Data availability

All data will be made available on the Pangaea data base (www.pangaea.de).

Acknowledgments

All scientific participants are thanked for shipboard collaboration in the data collection and post-cruise discussions and sample management. U1361 samples were provided by the Integrated Ocean Drilling Programme, Expedition 318. WEGA and MOGAM core samples were provided by the Italian “Programma Nazionale di Ricerche in

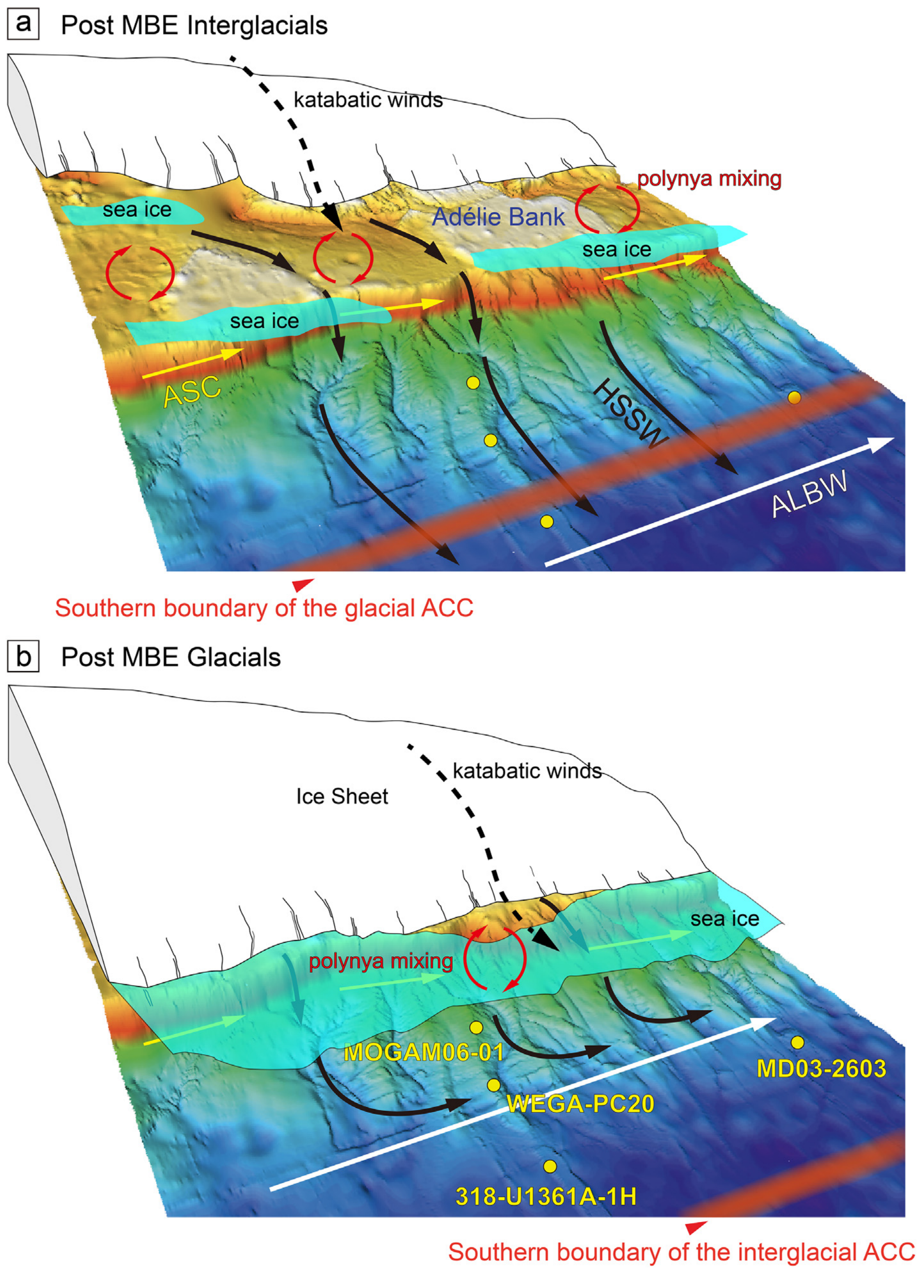

Fig. 10. Schematic representation of oceanographic and marine surface conditions during **a)** interglacials and **b)** glacials marine isotopic stages (MIS) between MIS 11 and MIS 5. Black arrows show the pathway of oxygenated High Salinity Shelf Water that feeds the Adélie Land Bottom Water during Post- Mid-Brunhes event interglacials. Red arrows represent polynya mixing. MBE: Mid-Bruhnes event (430 ka BP), HSSW: High salinity Shelf Water, Antarctic Slope Current (ASC), Antarctic Circumpolar Current: ACC, ALBW: Adélie Land Bottom Water.

Antartide”, Antarctic Expeditions 2000 and 2006. MD03-2603 core samples were provided by the Images X-CADO programme. MP acknowledges the EC Human Resources and Mobility Activity - Marie Curie European Re-Integration Grant (ERG) “HoloSed”, Contract 039566. CE and FJJE acknowledge funding from the Ministry of Science and Innovation Grants CTM2017-89711-C2-1-P co-financed by the European Regional Development Fund (FEDER). FJJE acknowledges JAMSTEC-MEXT support. RM was funded by the Royal Society Te Apārangi (NZ) Marsden Fund (18-VUW-089). CT-Scanning was carried out at the Division of Petrophysics of ENI, San Donato Milanese. This paper is a contribution to the SCAR PAIS Programme.

Appendix A. Supplementary data

Supplementary data to this article can be found online at https://doi.org/10.1016/j.gloplacha.2019.103045.

References

Abdi, H., 2007. The Bonferonni and Šidák corrections for multiple comparisons. In: Salkind, N. (Ed.), Encyclopedia of Measurement and Statistics. SAGE, Thousand Oaks (CA), pp. 103–109.

Adkins, J.F., 2013. The role of deep ocean circulation in setting glacial climates. Paleoceanography 28, 539–561.

Algeo, T.J., Maynard, J.B., 2004. Trace-element behavior and redox facies in core shales of Upper Pennsylvanian Kansas-type cyclothems. Chem. Geol. 206, 289–318.

Anderson, R.F., Ali, S., Bradtmiller, L.I., Nielsen, S.H.H., Fleisher, M.Q., Anderson, B.E., Burckle, L.H., 2009. Wind-driven upwelling in the Southern Ocean and the deglacial rise in atmospheric CO_2. Science 323, 1443–1448.

Aoki, S., Rintoul, S.R., Ushio, S., Watanabe, S., Bindoff, N.L., 2005. Freshening of the Adélie land bottom water near 140°E. Geophys. Res. Lett. 32, L23601. https://doi.org/10.1029/2005GL024246.

Aoki, S., Kitade, Y., Shimada, Ohshima, K.I., Tamura, T., Bajish, C.C., Moteki, M., Rintoul, S.R., 2013. Widespread freshening in the Seasonal Ice Zone near 140°E off the Adélie Land Coast, Antarctica, from 1994 to 2012. J. Geophys. Res.: Oceans 118, 6046–6063. https://doi.org/10.1002/2013JC009009.

Armand, L.K., Crosta, X., Romero, O., Pichon, J.J., 2005. The biogeography of major diatom taxa in Southern Ocean sediments: 1. Sea ice related species. Palaeogeogr. Palaeoclimatol. Palaeoecol. 223, 93–126.

Bahr, A., Jiménez-Espejo, F.J., Kolasinac, N., Grunert, P., Hernández-Molina, F.J., Röhl, U., Voelker, A., Escutia, C., Stow, D.A.W., Hodell, D., Alvarez-Zarikian, C.A., IODP Expedition 339 Scientists, 2014. Deciphering bottom current strength and paleoclimate signals from contourite deposits in the Gulf of Cádiz during the last 140 kyr: an inorganic geochemical approach. Geochem. Geophys. Geosyst. 15, 3145–3160. https://doi.org/10.1002/2014GC005356.

Baines, P.G., 2008. Mixing in downslope flows in the ocean — plumes versus gravity currents. Atmosphere-Ocean 46, 405–419.

Baines, P.G., Condie, S., 1998. Observations and modelling of antarctic downslope flows: a review. In: Jacobs, S.S., Weiss, R. (Eds.), Ocean, Ice and Atmosphere: Interactions at the Antarctic Continental Margin. 75. AGU Antarct. Res. Ser, pp. 29–49.

Beaman, R.J., 2011. A new high-resolution bathymetry model for the Terre Adelie and George V continental margin, East Antarctica. Antarct. Sci. 23, 95–103.

Bertram, R.A., Wilson, D.J., van de Flierdt, T., McKay, R.M., Jimenez-Espejo, F.J., Escutia, C., Duke, G., Taylor-Silva, B., Riesselman, C., 2018. Timescales and event sequences of middle to late Pliocene deglaciations in the Wilkes Subglacial Basin. Earth Planet. Sci. Lett. 494, 109–116.

Bindoff, N.L., Williams, G.D., Allison, I., 2001. Sea-ice growth and water mass modification in the Mertz Glacier Polynya, East Antarctica, during winter. Ann. Glaciol. 33, 399–406.

Borchers, A., Dietze, E., Kuhn, G., Esper, O., Voigt, I., Hartmann, K., Diekmann, B., 2016. Holocene ice dynamics and bottom-water formation associated with Cape Darnley polynya activity recorded in Burton Basin, East Antarctica. Mar. Geophys. Res. 37, 49–70.

Bostock, H.C., Sutton, P.J., Williams, M.J.M., Opdyke, B.N., 2013. Reviewing the circulation and mixing of Antarctic Intermediate Water in the South Pacific using evidence from geochemical tracers and Argo float trajectories. Deep-Sea Res. I Oceanogr. Res. Pap. 73, 84–98.

Brancolini, G., Harris, P.T., Shipboard party, 2000. Post-Cruise Report: Joint Italian/Australian marine geoscience expedition aboard the R.V. Tangaroa to the George Vth Land region of East Antarctica during February-March 2000. Australian Geol. Survey Organization Record 181 2000/19.

Brumsack, H.-J., 1989. Geochemistry of recent TOC-rich sediments from the Gulf of California and the Black Sea. Geol. Rundsch. 78, 851–882.

Busetti, M., Caburlotto, A., Armand, L., Damiani, D., Giorgetti, G., Lucchi, R.G., Quilty, P.G., Villa, G., 2003. Plio-Quaternary sedimentation on the Wilkes Land continental rise: preliminary results. Deep-Sea Res. II 50 (8–9), 1529–1562.

Caburlotto, A., De Santis, L., Camerlenghi, A., Dix, J.K., Zanolla, C., 2006. New insights into Quaternary glacial dynamic changes on the George Vth land continental margin (East Antarctica). Quat. Sci. Rev. 25, 3029–3049.

Caburlotto, A., Lucchi, R.G., De Santis, L., Macrı, P., Tolotti, R., 2009. Sedimentary processes on the Wilkes Land continental rise reflect changes in glacial dynamics and bottom water flow. Int. J. Earth Sci. 99, 909–926.

Calvert, S.E., Pedersen, T.F., 1993. Geochemistry of recent oxic and anoxic marine sediments: Implications for the geological record. Mar. Geol. 113, 67–88.

Calvert, S.E., Pedersen, T.F., 2007. Elemental proxies for palaeoclimatic and palaeoceanographic variability in marine sediments: interpretation and application. In: Hillaire-Marcel, C., De Vernal, A. (Eds.), Proxies in Late Cenozoic paleoceanography. Development in Marine Geology 1. pp. 567–644.

Campagne, P., Crosta, X., Houssais, M.N., Swingedouw, D., Schmidt, S., Martin, A., Devred, E., Capo, S., Marieu, V., Closset, I., Massé, G., 2015. Glacial ice and atmospheric forcing on the Mertz Glacier Polynya over the past 250 years. Nat. Commun. 6, 6642.

Canfield, D.E., Thamdrup, B., Hansen, J.W., 1993. The anaerobic degradation of organic matter in Danish coastal sediments: iron reduction, manganese reduction and sulfate reduction. Geochim. Cosmochim. Acta 57, 3867–3883.

Channell, J.E.T., Xuan, C., Hodell, D.A., 2009. Stacking paleointensity and oxygen isotope data for the last 1.5 Myr (PISO-1500). Earth Planet. Sci. Lett. 283 (1-4), 14–23.

Cook, C.P., van de Flierdt, T., Williams, T., Hemming, S.R., Iwai, M., Kobayashi, M., Jimenez-Espejo, F.J., Escutia, C., González, J.J., Khim, B.-K., McKay, R.M., Passchier, S., Bohaty, S.M., Riesselman, C.R., Tauxe, L., Sugisaki, S., Galindo, A.L., Patterson, M.O., Sangiorgi, F., Pierce, E.L., Brinkhuis, H., Klaus, A., Fehr, A., Bendle, J.P., Bijl, P.K., Carr, S., Dunbar, R.B., Flores, J.A., Hayden, T.G., Katsuki, K., Kong, G.S., Nakai, M., Olney, M.P., Pekar, S.F., Pross, J., Röhl, U., Sakai, T., Shrivastava, P.K., Stickley, C.E., Tuo, S., Welsh, K., Yamane, M., 2013. Dynamic behaviour of the East Antarctic ice sheet during Pliocene warmth. Nat. Geosci. 6, 765–769.

Cook, C.P., Hemming, S.R., van de Flierdt, T., Pierce Davis, E.L., Williams, T., Lopez Galindo, A., Jiménez Espejo, F.J., Escutia, C., 2017. Glacial erosion of East Antarctica in the Pliocene: a comparative study of multiple marine sediment provenance tracers. Chem. Geol. 466, 199–2018.

Cooper, A.K., O'Brien, P.E., Richter, C. (Eds.), 2004. Proc. ODP, Sci. Results, 188: College Station, TX (Ocean Drilling Program), https://doi.org/10.2973/odp.proc.sr.188.2004.

Croning, T.M., Dwyer, G.S., Caverly, E.K., Farmer, J., DeNinno, L.H., Rodriguez-Lazaro, J., Gemery, L., 2017. Enhanced Arctic amplification began at the Mid-Brunhes event ~400,000 years ago. Sci. Rep. 7, 14475.

Crespin, J., Yam, R., Crosta, X., Massé, G., Schmidt, S., Campagne, P., Shemesh, A., 2014. Holocene glacial discharge and recent instability in East Antarctica. Earth Planet. Sci. Lett. 394, 38–47.

Crosta, X., Koç, N., 2007. Diatoms: From micropaleontology to isotope geochemistry. In: Hilaire-Marcel, C., de Vernal, A. (Eds.), Proxies in Late Cenozoic Paleoceanography. Developments in Marine Geology Series Volume 1. Elsevier, Amsterdam, The Netherlands, pp. 327–369.

Crosta, X., Romero, O., Armand, L.K., Pichon, J.J., 2005. The biogeography of major diatom taxa in Southern Ocean sediments: 2 Open ocean related species. Palaeogeogr. Palaeoclimatol. Palaeoecol. 223, 66–92.

Crosta, X., Crespin, J., Swingedouw, D., Marti, O., Masson-Delmotte, V., Etourneau, J., Goosse, H., Braconnot, P., Yam, R., Brailovski, I., Shemesh, A., 2018. Ocean as the main driver of Antartic ice sheet retreat during the Holocene. Glob. Planet. Chang. 166, 62–74.

Damiani, D., Giorgetti, G., Memmi Turbani, I., 2006. Clay mineral fluctuations and surface textural analysis of quartz grains in Pliocene–Quaternary marine sediments from Wilkes Land continental rise (East-Antarctica): Paleoenvironmental significance. Mar. Geol. 226, 281–295.

Davison, W., Woof, C., Rigg, E., 1982. The dynamics of iron and manganese in a seasonally anoxin lake., direct measurement of fluxes using sediment traps. Limnol. Oceanogr. 27, 987–1003.

de Lange, G.J., 1998. Oxic vs. anoxic diagenetic alteration of turbiditic sediments in the Madeira Abyssal Plain, eastern North Atlantic. In: Weaver, P.P.E., Schmincke, H.-U., Firth, J.V., Duffield, W. (Eds.), Proceedings ODP. Scientific Results, 157 Ocean Drilling Program, College Station, TX, pp. 573–580.

De Santis and Expedition Scientists, 2006. XXI PNRA Expedition. *http://www.uta.enea.it/696-2/*.

De Santis, L., Brancolini, G., Donda, F., 2003. Seismo-stratigraphic analysis of the Wilkes Land continental margin (East Antarctica): influence of glacially-driven processes on the Cenozoic deposition. Deep-Sea Res. Pt II 50, 1563–1594.

De Santis, L., Brancolini, G., Accettella, D., Cova, A., Caburlotto, A., Donda, F., Pelos, C., Zgur, F., Presti, M., 2007. New insights into submarine geomorphology and depositional processes along the George V Land continental slope and upper rise (East Antarctica). In: Cooper, A.K., Raymond, C.R. (Eds.), Proceedings of the 10th ISAES X. USGS Open-File Report 2007, Extended Abstract.

Denis, D., Crosta, X., Barbara, L., Massé, G., Renssen, H., Ther, O., Giraudeau, J., 2010. Sea ice and wind variability during the Holocene in East Antarctica: Insight on middle high latitude coupling. Quat. Sci. Rev. 29, 3709–3719. https://doi.org/10.1016/j.quascirev.2010.08.007.

Donda, F., Brancolini, G., De Santis, L., Trincardi, F., 2003. Seismic facies and sedimentary processes on the continental rise off Wilkes Land (East Antarctica): evidence of bottom current activity. Deep-Sea Res. Pt II 50, 1509–1528.

Donda, F., Brancolini, G., O'Brien, P.E., De Santis, L., Escutia, C., 2007. Sedimentary processes in the Wilkes Land margin: a record of the Cenozoic East Antarctic Ice Sheet evolution. J. Geol. Soc. Lond. 164, 243–256.

EPICA community members, 2004. Eight glacial cycles from an Antarctic ice core. Nature 429, 623–628.

Escutia, C., Eittreim, S.L., Cooper, A.K., Nelson, C.H., 2000. Morphology and acoustic character of the Antarctic Wilkes Land turbidite systems: ice-sheet-sourced versus river-sourced fans. J. Sediment. Res. 70, 84–93.

Escutia, C., Nelson, C.H., Acton, G.D., Eittreim, S.L., Cooper, A.K., Warnke, D.A., Jaramillo, J.M., 2002. Current controlled deposition on the Wilkes Land continental rise, Antarctica. Geol. Soc. Lond. Mem. 22, 373–384.

Escutia, C., Warnke, D., Acton, G.D., Barcena, A., Burckle, L., Canals, M., Frazee, C.S., 2003. Sediment distribution and sedimentary processes across the Antarctic Wilkes Land margin during the Quaternary. Deep-Sea Res. Pt. II 50, 1481–1508.

Escutia, C., De Santis, L., Donda, F., Dunbar, R.B., Cooper, A.K., Brancolini, G., Eittreim, S.L., 2005. Cenozoic ice sheet history from East Antarctic Wilkes Land continental margin sediments. Glob. Planet. Chang. 45, 51–81.

Escutia, C., Bárcena, M.A., Lucchi, R.G., Romero, O., Ballegeer, A.M., Gonzalez, J.J., Harwood, D.M., 2009. Circum-Antarctic warming events between 4 and 3.5 Ma recorded in marine sediments from the Prydz Bay (ODP Leg 188) and the Antarctic Peninsula (ODP Leg 178) margins. Glob. Planet. Chang. 69, 170–184. https://doi.org/10.1016/j.gloplacha.2009.09.003.

Escutia, C., Brinkhuis, H., Klaus, A., and the Expedition 318 Scientists, 2011. Proceedings of the Integrated Ocean Drilling Program, 318. Tokyo (Integrated Ocean Drilling Program Management International, Inc.). doi: https://doi.org/10.2204/iodp.proc.318.109.2011.

Eusterhues, K., Heinrichs, H., Schneider, J., 2005. Geochemical response on redox fluctuations in Holocene lake sediments, Lake Steisslingen, Southern Germany. Chem. Geol. 222, 1–22.

Ferrari, R., Jansen, M.F., Adkins, J.F., Burke, A., Stewart, A.L., Thompson, F., 2014. Antarctic sea ice control on ocean circulation in present and glacial climates. Proc. Natl. Acad. Sci. U. S. A. 111, 8753–8758.

Fogwill, C.J., Turney, C.S.M., Golledge, N.R., Etheridge, D.M., Rubino, M., Thornton, D.P., Baker, A., Woodward, J., Winter, K., Van Ommen, T.D., Moy, A.D., 2017. Antarctic ice sheet discharge driven by atmosphere-ocean feedbacks at the Last Glacial Termination. Sci. Rep. 7, 39979.

Foster, T.D., Carmack, E.C., 1976. Frontal Zone mixing and Antarctic Bottom Water formation in the southern Weddell Sea. Deep-Sea Res. 23, 301–317.

Froelich, P.N., Klinkhammer, G.P., Bender, M.L., Luedtke, N.A., Heath, G.R., Cullen, D., Dauphin, P., Hammond, D., Hartman, B., Maynard, V., 1979. Early oxidation of organic matter in pelagic sediments of the eastern Equatorial Atlantic: suboxic diagenesis. Geochim. Cosmochim. Acta 43, 1075–1090.

Fukamachi, Y., Wakatsuchi, M., Taira, K., Kitagawa, S., Ushio, S., Takahashi, A., Oikawa, K., Furukawa, T., Yoritaka, H., Fukuchi, M., Yamanouchi, T., 2000. Seasonal variability of bottom water properties off Adélie Land, Antarctica. J. Geophys. Res. 105, 6531–6540.

Golledge, N., Kowalewski, D., Naish, T., Levy, R., Fogwill, C., Gasson, E., 2015. The multi-millennial Antarctic commitment to future sea-level rise. Nature 526, 421–425.

Guyodo, Y., Valet, J.-P., 1999. Global changes in intensity of the Earth's magnetic field during the past 800 kyr. Nature 399, 249–252.
Hammer, Ø., Harper, D.A.T., 2006. Paleontological Data Analysis. Blackwell 368 pp.
Hammer, Ø., Harper, D.A.T., Ryan, P.D., 2001. PAST: paleontological statistics software package for education and data analysis. Palaeontol. Electron. 4, 1–9.
Harris, P.T., Beaman, R.J., 2003. Processes controlling the formation of the Mertz Drift, George Vth continental shelf, East Antarctica: evidence from 3.5 kHz sub-bottom profiling and sediment cores. Deep-Sea Res. Pt II 50, 1463–1480.
Hepp, D.A., Moerz, T., Grutzner, J., 2006. Pliocene glacial cyclicity in a deep-sea sediment drift (Antarctic Peninsula Pacific Margin). Palaeogeogr. Palaeoclimatol. Palaeoecol. 231, 181–198.
Hillenbrand, C.-D., Camerlenghi, A., Cowan, E.A., Hernández-Molina, F.J., Lucchi, R.G., Rebesco, M., Uenzelmann-Neben, G., 2008. The present and past bottom-current flow regime around the sediment drifts on the continental rise west of the Antarctic Peninsula. Mar. Geol. 255, 50–63.
Hillenbrand, C.-D., Kuhn, G., Frederichs, T., 2009. Record of a Mid-Pleistocene depositional anomaly in West Antarctic continental margin sediments: an indicator for ice-sheet collapse? Quat. Sci. Rev. 28, 1147–1159.
Jaccard, S.L., Hayes, C.T., Martínez-García, A., Hodell, D.A., Anderson, R.F., Sigman, D.M., Haugh, G.H., 2013. Two modes of change in southern ocean productivity over the past million years. Science 339, 1419–1423. https://doi.org/10.1126/science.1227545.
Jaccard, S.L., Galbraith, E.D., Martínez-García, A., Anderson, R.F., 2016. Covariation of deep Southern Ocean oxygenation and atmospheric CO_2 through the last ice age. Nature 530, 207–210. https://doi.org/10.1038/nature16514.
Jakobsson, M., Løvlie, R., Al-Hanbali, H., Arnold, E., Backman, J., Mörth, M., 2000. Manganese and color cycles in Arctic Ocean sediments constrain Pleistocene chronology. Geology 28, 23–26.
Jimenez-Espejo, F.J., Martinez-Ruiz, F., Sakamoto, T., Iijima, K., Gallego-Torres, D., Harada, N., 2007. Paleoenvironmental changes in the western Mediterranean since the last glacial maximum: High resolution multiproxy record from the Algero-Balearic basin. Palaeogeogr. Palaeoclimatol. Palaeoecol. 246, 292–306. https://doi.org/10.1016/j.palaeo.2006.10.005.
Jolliffe, I.T., 1986. Principal Component Analysis. Springer-Verlag, New York.
Jouzel, J., Masson-Delmotte, V., Cattani, O., Dreyfus, G., Falourd, S., Hoffmann, G., Minster, B., Nouet, J., Barnola, J.M., Chappellaz, J., Fischer, H., Gallet, J.C., Johnsen, S., Leuenberger, M., Loulergue, L., Luethi, D., Oerter, H., Parrenin, F., Raisbeck, G., Raynaud, D., Schilt, A., Schwander, J., Selmo, E., Souchez, R., Spahni, R., Stauffer, B., Steffensen, J.P., Stenni, B., Stocker, T.F., Tison, J.L., Werner, M., Wolff, E.W., 2007. Orbital and millennial Antarctic climate variability over the past 800,000 years. Science 317, 793–796. https://doi.org/10.1126/science.1141038.
Jung, M., Ilmberger, J., Mangini, A., Emeis, K.-C., 1997. Why some Mediterranean sapropels survived burn-down (and others did not). Mar. Geol. 141, 51–60.
Kaboth-Bahr, S., Denis, V., Su, C.-C., O'Regan, M., Gyllencreutz, R., Jakobsson, M., Löwemark, L., 2018. Deciphering ~45.000 years of Arctic Ocean lithostratigraphic variability through multivariate statistical analysis. Quat. Int. https://doi.org/10.1016/j.quaint.2018.11.043. *in press*.
Kohfeld, K.E., Chase, Z., 2017. Temporal evolution of mechanisms controlling ocean carbon uptake during the last glacial cycle. Earth Planet. Sci. Lett. 472, 206–215.
Korff, L., von Dobeneck, T., Frederichs, T., Kasten, S., Kuhn, G., Gersonde, R., Diekmann, B., 2016. Cyclic magnetite dissolution in Pleistocene sediments of the abyssal northwest Pacific Ocean: Evidence for glacial oxygen depletion and carbon trapping. Paleoceanography 31, 600–624. https://doi.org/10.1002/2015PA002882.
Krueger, S., Leuschner, D.C., Ehrmann, W., Schmiedl, G., Mackensen, A., 2012. North Atlantic Deep Water and Antarctic Bottom Water variability during the last 200 ka recorded in an abyssal sediment core off South Africa. Glob. Planet. Chang. 80-81, 180–189.
Lacarra, M., Houssais, M.N., Herbaut, C., Sultan, E., Beauverger, M., 2014. Dense shelf water production in the Adélie Depression 2004-2012: impact of the Mertz glacier calving. J. Geoph. Res. 119, 5203–5220.
Laj, C., Channell, J.E.T., 2007. Geomagnetic excursions. Treatise Geophys. 5, 373–416.
Lisiecki, L.E., Raymo, M.E., 2005. A Pliocene–Pleistocene stack of 57 globally distributed benthic δ18O records. Paleoceanography 20 PA1003.
Löwemark, L., Jakobsson, M., Mörth, M., Backman, J., 2008. Arctic Ocean manganese contents and sediment colour cycles. Polar Res. 27, 105–113. https://doi.org/10.1111/j.1751-8369.2008.00055.x.
Lucchi, R.G., Rebesco, M., 2007. Glacial contourites on the Antarctic Peninsula margins: insight for palaeoenvironmental and palaeoclimatic conditions. In: Economic and Palaeosignificance of Contourite Deposits. In: Viana, A.R., Rebesco, M. (Eds.), Geological Society of London special publication 276, pp. 111–127.
Lucchi, R.G., Rebesco, M., Camerlenghi, A., Busetti, M., Tomadin, L., Villa, G., Persico, D., Morigi, C., Bonci, M.C., Giorgetti, G., 2002. Glacimarine Sedimentary Processes of a high-latitude, deep-sea sediment drift (Antarctic Peninsula Pacific margin). Mar. Geol. 189, 343–370.
Lucchi, R.G., Camerlenghi, A., Rebesco, M., Colmenero-Hidalgo, E., Sierro, F.J., Sagnotti, L., Urgeles, R., Melis, R., Morigi, C., Barcena, M.-A., Giorgetti, G., Villa, G., Persico, D., Flores, J.-A., Rigual-Hernandez, A.S., Pedrosa, M.T., Macrì, P., Caburlotto, A., 2013. Postglacial sedimentary processes on the Storfjorden and Kveithola trough mouth fans: Significance of extreme glacimarine sedimentation. Glob. Planet. Chang. 111, 309–326.
Lucchi, R.G., Sagnotti, L., Camerlenghi, A., Macrì, P., Rebesco, M., Pedrosa, M.T., Giorgetti, G., 2015. Marine sedimentary record of Meltwater Pulse 1a in the NW Barents Sea continental margin. Arktos 1, 7. https://doi.org/10.1007/s41063-015-0008-6.
Lüthi, D., Le Floch, M., Bereiter, B., Blunier, T., Barnola, J.-M., Siegenthaler, U., Raynaud, D., Jouzel, J., Fischer, H., Kawamura, K., Stocker, T.F., 2008. High-resolution carbon dioxide concentration record 650,000–800,000 years before present. Nature 453, 379–382. https://doi.org/10.1038/nature06949.
Lyons, T.W., Werne, J.P., Hollander, D.J., Murray, R.W., 2003. Contrasting sulfur geochemistry and Fe/Al and Mo/Al ratios across the last oxic-to-anoxic transition in the Cariaco Basin, Venezuela. Chem. Geol. 195, 131–157.
Mackensen, A., Rudolph, M., Kuhn, G., 2001. Late Pleistocene deep-water circulation in the subantarctic eastern Atlantic. Glob. Planet. Chang. 30, 197–229.
Macrì, P., Sagnotti, L., Dinares-Turrel, J., Caburlotto, A., 2005. A composite record of Late Pleistocene relative geomagnetic paleointensity from the Wilkes Land Basin (Antarctica). Phys. Earth Planet. Inter. 151, 223–242.
Macrì, P., Sagnotti, L., Lucchi, R.G., Rebesco, M., 2006. A stacked record of relative geomagnetic paleointensity for the last 270 ka from sedimentary sequences on the western continental rise of the Antarctic Peninsula. Earth Planet. Sci. Lett. 252, 162–179.
Mangini, A., Jung, M., Laukenmann, S., 2001. What do we learn from peaks of uranium and of manganese in deep sea sediments? Mar. Geol. 177, 63–78.
Mantyla, A.W., Reid, J.L., 1983. Abyssal characteristics of the Worlds Ocean Waters. Deep-Sea Res 30, 805–833.
März, C., Stratmann, A., Matthiessen, J., Meinhardt, A.-K., Eckert, S., Schnetger, B., Vogt, C., Stein, R., Brumsack, H.-J., 2011. Manganese-rich brown layers in Arctic Ocean sediments: composition, formation mechanisms, and diagenetic overprint. Geochim. Cosmochim. Acta 75, 7668–7687.
McLaren, J.W., Berman, S.S., Boyko, V.J., Russell, D.S., 1981. Simultaneous determination of major, minor, and trace elements in marine sediments by inductively coupled plasma atomic emission spectrometry. Anal. Chem. 53, 1802–1806.
McLennan, S.M., 2001. Relationships between the trace element composition of sedimentary rocks and upper continental crust. Geochem. Geophys. Geosyst. 2https://doi.org/10.1029/2000GC000109. 2000GC000109.
McManus, J., Berelson, W.M., Klinkhammer, G.P., Hammond, D.E., Holm, C., 2005. Authigenic uranium: relationship to oxygen penetration depth and organic carbon rain. Geochim. Cosmochim. Acta 69, 95–108.
Meckler, A.N., Sigman, D.M., Gibson, K.A., François, R., Martínez-Garcia, A., Jaccard, S.L., Röhl, U., Peterson, L.C., Tiedemann, R., Haug, G.H., 2013. Deglacial pulses of deep-ocean silicate into the subtropical North Atlantic Ocean. Nature 495, 495–499.
Michel, E., Crosta, X., 2003. MD 130 / CADO cruise. RV Marion Dufresne. https://doi.org/10.17600/3200040.
Miles, B.W.J., Stokes, C.R., Vieli, A., Cox, N.J., 2013. Rapid, climate-driven changes in outlet glaciers on the Pacific coast of East Antarctica. Nature 500, 563–566.
Monien, D., Kuhn, G., von Eynatten, H., Talarico, F.M., 2012. Geochemical provenance analysis of fine-grained sediment revealing Late Miocene to recent Paleo-Environmental changes in the Western Ross Sea, Antarctica. Glob. Planet. Change 96–97, 41–58.
Morford, J.L., Emerson, S., 1999. The geochemistry of redox sensitive trace metals in sediments. Geochim. Cosmochim. Acta 63, 1735–1750.
Nameroff, T.J., Calvert, S.E., Murray, J.W., 2004. Glacial–interglacial variability in the eastern tropical North Pacific oxygen minimum zone recorded by redox-sensitive trace metals. Paleoceanography 19, PA1010. https://doi.org/10.1029/2003PA000912.
Patterson, M.O., McKay, R., Naish, T., Escutia, C., Jimenez-Espejo, F.J., Raymo, M.E., Meyers, S.R., Tauxe, L., Brinkhuis, H., IODP Expedition 318 Scientists, 2014. Orbital forcing of the East Antarctic ice sheet during the Pliocene and Early Pleistocene. Nat. Geosci. 7, 841–847.
Pedro, J.B., Martin, T., Steig, E.J., Jochum, M., Park, W., Rasmussen, S.O., 2016. Southern Ocean deep convection as a driver of Antarctic warming events. Geophys. Res. Lett. 43, 2192–2199. https://doi.org/10.1002/2016GL067861.
Piper, D.Z., Perkins, R.B., 2004. A modern vs. Permian black shale- the hydrography, primary productivity, and water-column chemistry of deposition. Chem. Geol. 206, 177–197.
Presti, M., De Santis, L., Busetti, M., Harris, P., 2003. Late Pleistocene-Holocene sedimentation in the George V Basin, Antarctica as recorded by a sediment drift deposit. In: Deep Sea Research Special Volume II, 50, Issues 8-9. In: Harris, P., Brancolini, G., Bindoff, N., De Santis, L. (Eds.), Recent investigations of the Mertz Polynya and George Vth Land continental margin, East Antarctica. Elsevier Publ, pp. 1441–1461 (ISSN: 0967-0645).
Presti, M., De Santis, L., Brancolini, G., Harris, P.T., 2005. Continental shelf record of the East Antarctic Ice Sheet evolution: seismo-stratigraphic evidence from the George V Basin. Quat. Sci. Rev. 10-11, 1223–1241.
Presti, M., Barbara, L., Denis, D., Schmidt, S., De Santis, L., Crosta, X., 2011. Sediment delivery and depositional patterns off Adélie Land (East Antarctica) in relation to late Quaternary climatic cycles. Mar. Geol. 284, 96–113.
Purkey, S.G., Johnson, G.C., 2012. Global contraction of Antarctic Bottom Water between the 1980s and 2000s. J. Clim. 25, 5830–5844.
Reinardy, B.T.I., Escutia, C., Iwai, M., Jimenez-Espejo, F.J., Cook, C., van de Flierdt, T., Brinkhuis, H., 2015. Repeated advance and retreat of the East Antarctic Ice Sheet on the continental shelf during the early Pliocene warm period. Palaeogeogr. Palaeoclimatol. Palaeoecol. 422, 65–84.
Reitz, A., Hensen, C., Kasten, S., Funk, J.A., De Lange, G.J., 2004. A combined geochemical and rock-magnetic investigation of a redox horizon at the last glacial/interglacial transition. Phys. Chem. Earth 29, 921–931.
Richter, T.O., Van der Gaast, S., Koster, B., Vaars, A., Gieles, R., De Stitger, H., De Haas, H., Van Weering, T.C.E., 2006. The Avaatech XRF core scanner: technical description and applications to NE Atlantic sediments. In: Rothwell, R.G. (Ed.), New Techniques in Sediment Core Analysis. Geological Society of London Special Publications 267pp. 29–50.
Rignot, E., Mouginot, J., Scheuchl, B., van den Broeke, M., van Wessem, M.J., Morlighem, M., 2019. Four decades of Antarctic Ice Sheet mass balance from 1979-2017. Proc.

Natl. Acad. Sci. 116, 1095–1103. https://doi.org/10.1073/pnas.1812883116.
Rintoul, S.R., 1998. On the origin and influence of Adélie Land bottom water. In: Ocean, Ice and Atmosphere: Interactions at the Antarctic Continental Margin. American Geophysical Union, Washington DC, pp. 151–171.
Rintoul, S.R., 2007. Rapid freshening of Antarctic Bottom Water formed in the Indian and Pacific Oceans. Geophys. Res. Lett. 34, L06606. https://doi.org/10.1029/2006GL028550.
Ritz, C., Edwards, T.L., Durand, G., Payne, A.J., Peyaud, V., Hindmarsh, R.C., 2015. Potential sea-level rise from Antarctic ice-sheet instability constrained by observations. Nature 528, 115–118.
Rodrigo-Gámiz, M., Martínez-Ruiz, F., Rodríguez-Tovar, F.J., Jiménez-Espejo, F.J., Pardo-Igúzquiza, E., 2014. Millennial- to centennial-scale climate periodicities and forcing mechanisms in the westernmost Mediterranean for the past 20,000 yr. Quat. Res. 81, 78–93.
Rodrigues, T., Alonso-García, M., Hodell, D.A., Rufino, M., Naughton, F., Grimalt, J.O., Voelker, A.H.L., Abrantes, F., 2017. A 1-Ma record of sea surface temperature and extreme cooling events in the North Atlantic: A perspective from the Iberian margin. Quat. Sci. Rev. 172, 118–130.
Ronge, T.A., Steph, S., Tiedemann, R., Prange, M., Merkel, U., Nürnberg, D., Kuhn, G., 2015. Pushing the boundaries: Glacial/interglacial variability of intermediate and deep waters in the southwest Pacific over the last 350,000 years. Paleoceanography 30, 23–38. https://doi.org/10.1002/2014PA002727.
Rutten, A., de Lange, G.J., Hayes, A., Rohling, E.J., de Jong, A.F.M., van der Borg, K., 1999. Deposition of sapropel S1 sediments in oxic pelagic and anoxic brine environments in the Eastern Mediterranean: Differences in diagenesis and preservation. Mar. Geol. 153, 319–335.
Sageman, B.B., Murphy, A.E., Werne, J.P., Ver Straeten, C.A., Hollander, D.J., Lyons, T.W., 2003. A tale of shales: the relative roles of production, decomposition, and dilution in the accumulation of organic-rich strata, Middle–Upper Devonian, Appalachian Basin. Chem. Geol. 195, 229–273.
Sen Gupta, A., Santoso, A., Taschetto, A.S., Ummenhofer, C.C., Trevena, J., England, M.H., 2009. Projected changes to the Southern Hemisphere ocean and sea ice in the IPCC AR4 climate models. J. Clim. 22, 3047–3078.
Shen, Q., Wang, H., Shum, C.K., Jiang, L., Hsu, H.T., Dong, J., 2018. Recent high-resolution Antarctic ice velocity maps reveal increased mass loss in Wilkes Land, East Antarctica. Sci. Rep. 8, 4477.
Tauxe, L., Stickley, C.E., Sugisaki, S., Bijl, P.K., Bohaty, S.M., Brinkhuis, H., Escutia, C., Flores, J., Houben, A.J.P., Iwai, M., Jimenez-Espejo, F., McKay, R., Passchier, S., Pross, J., Riesselman, C.R., Rohl, U., Sangiorgi, F., Welsh, K., Klaus, A., Fehr, A., Bendle, J.A.P., Dunbar, R., Gonzolez, J., Hayden, T., Katsuki, K., Olney, M.P., Pekar, S.F., Shrivastava, P.K., Van de Flierdt, T., Williams, T., Yamane, M., 2012. Chronostratigraphic framework for the IODP Expedition 318 cores from the Wilkes Land Margin: Constraints for paleoceanographic reconstruction. Paleoceanography 27, 19.
Thomson, J., Higgs, J.N.C., Wilson, T.R.S., Croudace, IW., de Lange, G.J., Van Santvoort, P.J.M., 1995. Redistribution and geochemical behaviour of redox-sensitive elements around S1, the most recent eastern Mediterranean sapropel. Geochim. Cosmochim. Acta 59, 3487–3501.
Tjallingii, R., Röhl, U., Kölling, M., Bickert, T., 2007. Influence of the water content on X-ray fluorescence core-scanning measurements in soft marine sediments. Geochem. Geophys. Geosyst. 8. https://doi.org/10.1029/2006GC001393.
Tolotti, R., Bárcena, M.A., Macrì, P., Caburlotto, A., Bonci, M.C., De Santis, L., Donda, F., Corradi, N., Crosta, X., 2017. Wilkes land late pleistocene diatom age model: from bio-events to quantitative biostratigraphy. Rev. Micropaleontol. 61, 81–96. https://doi.org/10.1016/j.revmic.2018.05.001.
Tribovillard, N., Algeo, T.J., Lyons, T., Riboulleau, A., 2006. Trace metals as paleoredox and paleoproductivity proxies: an update. Chem. Geol. 232, 12–32.
Van der Weijden, C.H., 2002. Pitfalls of normalization of marine geochemical data using a common divisor. Mar. Geol. 184, 167–187.
Van Santvoort, P.J.M., De Lange, G.J., Thomson, J., Cussen, H., Wilson, T.R.S., Krom, M.D., Strohle, K., 1996. Active post-depositional oxidation of the most recent sapropel (S1) in the eastern Mediterranean. Geochim. Cosmochim. Acta 60, 4007–4024.
Wagner, M., Henry, I.L., 2017. Trace metal evidence for a poorly ventilated glacial Southern Ocean. Quarter. Sci. Rev. 170, 109–120.
Weltje, G.J., Tjallingii, R., 2008. Calibration of XRF core scanners for quantitative geochemical logging of sediment cores: Theory and application. Earth Planet. Sci. Lett. 274, 423–438.
Williams, G.D., Bindoff, N.L., 2003. Winter time oceanography of the Adelie Depression. Deep-Sea Res. Pt II 50, 1373–1392.
Williams, G.D., Aoki, S., Jacobs, S.S., Rintoul, S.R., Tamura, T., Bindoff, N.L., 2010. Antarctic bottom water from the Adélie and George V Land coast, East Antarctica (140°–149°E). J. Geophys. Res. 115, C04027. https://doi.org/10.1029/2009JC005812.
Williams, G.D., Herraiz-Borreguero, L., Roquet, F., Tamura, T., Ohshima, K.I., Fukamachi, Y., Fraser, A.D., Gao, L., Chen, H., McMahon, C.R., Harcourt, R., Hindell, M., 2016. The suppression of Antarctic bottom water formation by melting ice shelves in Prydz Bay. Nat. Commun. 7, 12577.
Yarincik, K.M., Murray, R.W., Lyons, T.W., Peterson, L.C., Haug, G.H., 2000. Oxygenation history of bottom waters in the Cariaco Basin, Venezuela, over the past 578,000 years: Results from redox-sensitive metals (Mo, V, Mn, and Fe). Paleoceanography 15, 593–604.
Yin, Q.Z., Berger, A., 2010. Insolation and CO_2 contribution to the interglacial climate before and after the Mid-Brunhes Event. Nat. Geosci. 3, 243–246.
Zielinski, U., Gersonde, R., 2002. Plio-Pleistocene diatom biostratigraphy from ODP Leg 177, Atlantic sector of the Southern Ocean. Mar. Micropaleontol. 45, 225–268.